



The Sixth Data Release of the Radial Velocity Experiment (RAVE). I. Survey Description, Spectra, and Radial Velocities

Matthias Steinmetz¹ , Gal Matijević¹ , Harry Enke¹ , Tomaž Zwitter² , Guillaume Guiglion¹ , Paul J. McMillan³ , Georges Kordopatis⁴ , Marica Valentini¹ , Cristina Chiappini¹ , Luca Casagrande⁵ , Jennifer Wojno⁶ , Borja Anguiano⁷ , Olivier Bienaymé⁸ , Albert Bijaoui⁴, James Binney⁹ , Donna Burton^{10,11} , Paul Cass¹⁰ , Patrick de Laverny⁴ , Kristin Fiegert¹⁰ , Kenneth Freeman⁵ , Jon P. Fulbright⁶, Brad K. Gibson¹² , Gerard Gilmore¹³ , Eva K. Grebel¹⁴ , Amina Helmi¹⁵ , Andrea Kunder¹⁶ , Ulisse Munari¹⁷ , Julio F. Navarro¹⁸, Quentin Parker^{19,20} , Gregory R. Ruchi⁶ , Alejandra Recio-Blanco⁴, Warren Reid^{21,22}, George M. Seabroke²³ , Alessandro Siviero²⁴, Arnaud Siebert⁸, Milorad Stupar^{10,22} , Fred Watson²⁵ , Mary E. K. Williams¹, Rosemary F. G. Wyse^{6,26} , Friedrich Anders^{1,27} , Teresa Antoja²⁷ , Danijela Birko² , Joss Bland-Hawthorn²⁸ , Diego Bossini²⁹ , Rafael A. García^{30,31} , Ismael Carrillo¹ , William J. Chaplin^{32,33} , Yvonne Elsworth^{32,33}, Benoit Famaey⁸ , Ortwin Gerhard³⁴ , Paula Jofre³⁵ , Andreas Just¹⁴ , Savita Mathur^{36,37} , Andrea Miglio³³ , Ivan Minchev¹ , Giacomo Monari^{1,8}, Benoit Mosser³⁸ , Andreas Ritter²⁰, Thaise S. Rodrigues¹⁷ , Ralf-Dieter Scholz¹ , Sanjib Sharma²⁸ , and Kseniia Sysoliatina¹⁴

(The RAVE collaboration)

¹ Leibniz-Institut für Astrophysik Potsdam (AIP), An der Sternwarte 16, D-14482 Potsdam, Germany; msteinmetz@aip.de

² University of Ljubljana, Faculty of Mathematics and Physics, Jadranska 19, SI-1000 Ljubljana, Slovenia

³ Lund Observatory, Department of Astronomy and Theoretical Physics, Lund University, Box 43, SE-22100 Lund, Sweden

⁴ Université Côte d'Azur, Observatoire de la Côte d'Azur, CNRS, Laboratoire Lagrange, France

⁵ Research School of Astronomy & Astrophysics, The Australian National University, Canberra, Australia

⁶ The Johns Hopkins University, Department of Physics and Astronomy, 3400 N. Charles St., Baltimore, MD 21218, USA

⁷ Department of Astronomy, University of Virginia, Charlottesville, VA 22904, USA

⁸ Observatoire astronomique de Strasbourg, Université de Strasbourg, CNRS, 11 rue de l'Université, F-67000 Strasbourg, France

⁹ Rudolf Peierls Centre for Theoretical Physics, Clarendon Laboratory, Parks Rd., Oxford OX1 3PU, UK

¹⁰ Australian Astronomical Observatory, Siding Spring, Coonabarabran NSW 2357, Australia

¹¹ University of Southern Queensland (USQ), West St. Toowoomba Qld 4350 Australia

¹² E.A. Milne Centre for Astrophysics, University of Hull, Hull HU6 7RX, UK

¹³ Institute of Astronomy, Cambridge, UK

¹⁴ Astronomisches Rechen-Institut, Zentrum für Astronomie der Universität Heidelberg, Mönchhofstr. 12–14, D-69120 Heidelberg, Germany

¹⁵ Kapteyn, Astronomical Institute, University of Groningen, P.O. Box 800, 9700 AV Groningen, The Netherlands

¹⁶ Saint Martin's University, 5000 Abbey Way SE, Lacey, WA 98503, USA

¹⁷ INAF Astronomical Observatory of Padova, I-36012 Asiago (VI), Italy

¹⁸ Department of Physics and Astronomy, University of Victoria, Victoria, BC, V8P5C2, Canada

¹⁹ CYM Physics Building, The University of Hong Kong, Pokfulam, Hong Kong SAR, People's Republic of China

²⁰ The Laboratory for Space Research, Hong Kong University, Cyberport 4, Hong Kong SAR, People's Republic of China

²¹ Department of Physics and Astronomy, Macquarie University, Sydney, NSW 2109, Australia

²² Western Sydney University, Locked bag 1797, Penrith South, NSW 2751, Australia

²³ Mullard Space Science Laboratory, University College London, Holmbury St Mary, Dorking, RH5 6NT, UK

²⁴ Dipartimento di Fisica e Astronomia G. Galilei, Università di Padova, Vicolo dell'Osservatorio 3, I-35122, Padova, Italy

²⁵ Department of Industry, Science, Energy and Resources, 105 Delhi Rd., North Ryde, NSW 2113, Australia

²⁶ Kavli Institute for Theoretical Physics, University of California, Santa Barbara, CA 93106, USA

²⁷ Institut de Ciències del Cosmos, Universitat de Barcelona (IEEC-UB), Martí i Franquès 1, E-08028 Barcelona, Spain

²⁸ Sydney Institute for Astronomy, School of Physics, The University of Sydney, NSW 2006, Australia

²⁹ Instituto de Astrofísica e Ciências do Espaço, Universidade do Porto, CAUP, Rua das Estrelas, 4150-762 Porto, Portugal

³⁰ IRFU, CEA, Université Paris-Saclay, F-91191 Gif-sur-Yvette, France

³¹ AIM, CEA, CNRS, Université Paris-Saclay, Université Paris Diderot, Sorbonne Paris Cité, F-91191 Gif-sur-Yvette, France

³² School of Physics and Astronomy, University of Birmingham, Edgbaston, Birmingham B15 2TT, UK

³³ Stellar Astrophysics Centre (SAC), Department of Physics and Astronomy, Aarhus University, DK-8000 Aarhus C, Denmark

³⁴ Max-Planck-Institut für extraterrestrische Physik, Postfach 1312, Giessenbachstr., D-85741 Garching, Germany

³⁵ Núcleo de Astronomía, Facultad de Ingeniería y Ciencias, Universidad Diego Portales, Ejército 441, Santiago de Chile, Chile

³⁶ Instituto de Astrofísica de Canarias, La Laguna, Tenerife, Spain

³⁷ Dpto. de Astrofísica, Universidad de La Laguna, La Laguna, Tenerife, Spain

³⁸ LESIA, Observatoire de Paris, PSL Research University, CNRS, Sorbonne Université, Université Paris Diderot, F-92195 Meudon, France

Received 2020 February 9; revised 2020 June 6; accepted 2020 June 8; published 2020 July 27

Abstract

The Radial Velocity Experiment (RAVE) is a magnitude-limited ($9 < I < 12$) spectroscopic survey of Galactic stars randomly selected in Earth's southern hemisphere. The RAVE medium-resolution spectra ($R \sim 7500$) cover the Ca-triplet region (8410–8795 Å). The sixth and final data release (DR6) is based on 518,387 observations of 451,783 unique stars. RAVE observations were taken between 2003 April 12 and 2013 April 4. Here we present the genesis, setup, and data reduction of RAVE as well as wavelength-calibrated and flux-normalized spectra and error spectra for all observations in RAVE DR6. Furthermore, we present derived spectral classification and radial velocities for the RAVE targets, complemented by cross-matches with Gaia DR2 and other relevant catalogs. A comparison between internal error estimates, variances derived from stars with more than one observing epoch, and a comparison with radial velocities of Gaia DR2 reveals consistently that 68% of the objects have a velocity

accuracy better than 1.4 km s^{-1} , while 95% of the objects have radial velocities better than 4.0 km s^{-1} . Stellar atmospheric parameters, abundances and distances are presented in a subsequent publication. The data can be accessed via the RAVE website (<http://rave-survey.org>) or the VizieR database.

Unified Astronomy Thesaurus concepts: [Stellar populations \(1622\)](#); [Galaxy stellar content \(621\)](#); [Milky Way Galaxy \(1054\)](#); [Milky Way dynamics \(1051\)](#); [Surveys \(1671\)](#); [Sky surveys \(1464\)](#); [Catalogs \(205\)](#)

1. Introduction

Deciphering the structure and formation history of the Galaxy provides important clues for understanding galaxy formation in a broader context. Wide-field spectroscopic surveys play a particularly important role in the analysis of the Milky Way: spectroscopy enables a measure of a star's radial velocity (RV), one of the six-dimensional coordinates of position and velocity, which in turn allows us to study the details of Galactic dynamics. Spectroscopy also permits a measure of the abundances of chemical elements in a star's atmosphere, which holds important clues to the star's initial chemical composition and the subsequent metal enrichment of the interstellar medium traced by stars of different ages and metallicities (see, e.g., Freeman & Bland-Hawthorn 2002; Bland-Hawthorn & Gerhard 2016). However, despite the importance of stellar spectroscopy for Galactic dynamics and Galactic archeology, the data situation in the early 2000s was far from satisfactory. RVs were listed for some 50,000 stars in the databases of the Centre de Données astronomiques de Strasbourg (CDS), an astonishingly small number compared to the approximately one million spectra available for galaxy redshifts listed at that time. Furthermore, these RVs and their underlying spectra comprised a very heterogeneous sample in terms of selection, resolution, epoch, or signal-to-noise ratio (S/N). The situation changed somewhat with the advent of the Geneva Copenhagen survey (Nordström et al. 2004), which provided RVs, effective temperatures, and metallicities for a homogeneous sample of 14,139 stars. However, this sample covered only a sphere of about 100 pc radius around the Sun (the so-called Hipparcos sphere).

The RADial Velocity Experiment (RAVE) was originally set up as a pilot survey using the existing 6dF multi-object spectrograph at AAO's UK Schmidt telescope (UKST) to observe about 100,000 stars in ~ 180 nights of unscheduled bright time during the years 2003–2005 (Steinmetz 2003). Spectra were to be taken covering the infrared Ca triplet region also employed by the Gaia RVS system (see Recio-Blanco et al. 2016). Motivated also by the astrometric satellite mission concepts *Deutsches Interferometer für Vielkanalphotometrie und Astrometrie* (DIVA; Bastian et al. 2001) and Full-sky Astrometric Mapping Explorer (FAME; Johnston 2003), this pilot survey was intended as a pathfinder for a considerably larger campaign targeting up to 40 million targets using a new Echidna-based multi-object spectrograph for the UKST, thus providing a vast kinematic database three orders of magnitude larger than any other survey planned in this period. While the DIVA and FAME missions were terminated in 2004, the results of the RAVE pilot survey were very encouraging. In particular, in addition to RVs, the determination of relevant information on stellar atmospheric parameters and potentially even abundance ratios appeared feasible. Consequently RAVE was continued for, eventually, a full 10 year period, providing one of the largest databases for stellar parameters and RVs. Meanwhile

a series of five data releases (DRs) with an increasing number of targets and increasingly refined data products have been released: DR1 (Steinmetz et al. 2006) provided RVs derived from 25,274 spectra; DR2 (Zwitter et al. 2008) provided RVs and atmospheric parameters derived from 51,829 spectra; DR3 (Siebert et al. 2011) provided the full pilot survey with 83,072 spectra; DR4 (Kordopatis et al. 2013) employed a new and much more refined pipeline for stellar parameter determination, and provided RVs and stellar parameters based on 482,430 spectra; DR5 (Kunder et al. 2017) provided a new and enhanced calibration of the derived stellar parameters, included a new calibration of giant stars based on information from the asteroseismic K2 mission, and linked RAVE targets to the Tycho–Gaia astrometric solution of Gaia DR1 (Lindegren et al. 2016). The RAVE data releases were complemented by value added catalogs, including spectro-photometric distances (Breddels et al. 2010; Zwitter et al. 2010; Burnett et al. 2011; Binney et al. 2014; McMillan et al. 2018), chemical abundances (Boeche et al. 2011; Casey et al. 2017), and automated spectral classification (Matijević et al. 2012) as well as catalogs of active stars (Žerjal et al. 2013, 2017) and of candidates for very metal-poor stars (Matijević et al. 2017). Furthermore, RAVE has meanwhile been complemented by surveys of similar or even larger size at lower (e.g., SEGUE, Yanny et al. 2009; LAMOST, Zhao et al. 2012) and higher spectral resolution (e.g., APOGEE, Majewski et al. 2017; GALAH, De Silva et al. 2015; Gaia–ESO, Gilmore et al. 2012). For a recent review on abundances derived from large spectroscopic surveys we refer to Jofré et al. (2019).

The pair of this paper (DR6-1) and its accompanying paper (DR6-2; Steinmetz et al. 2020) is the sixth and last publication in the series of RAVE data release papers. DR6-1 will focus on the spectra taken and is accompanied by a database of wavelength-calibrated and flux-normalized spectra for 518,387 observations of 451,783 unique stars. DR6-2 provides a new set of stellar parameters employing parallax information from Gaia DR2 (Gaia Collaboration et al. 2018), a robust $[\alpha/\text{Fe}]$ ratio, and individual $[\text{Fe}/\text{H}]$, $[\text{Al}/\text{H}]$, and $[\text{Ni}/\text{H}]$ ratios.

DR6-1 is structured as follows: in Section 2 we give an overview of the survey facility and performance. We outline the data reduction and provide direct references to sections of previous papers where the interested reader can find further details. Section 3 presents the spectra in the RAVE spectral catalog, which we are releasing here for the first time, and the reduction procedure of the RAVE raw data. Section 4 presents the automated classification of RAVE spectra. Section 5 is devoted to the derivation of RVs. RAVE data validation including a comparison of RAVE RVs with Gaia DR2 data is done in Section 6. Section 7 presents the RAVE spectral DR6 catalog, RVs, classification, and cross-match with other relevant catalog data. Finally, Section 7 gives a summary, draws some conclusions, and provides an outlook.

2. Survey Description

Most of the technical specification and description of the Survey performance in terms of observational setup, procedure, and data reduction are outlined in the DR1–DR5 data release papers. Since this paper describes the final data release, we give an overview of the basic survey procedures and provide references to the sections in previous papers where the interested reader can find further details.

2.1. Survey Facility

RAVE observations were performed at the 1.23 m UK Schmidt telescope at Siding Spring in Australia using the 6dF multi-object spectrograph (Watson et al. 2000), featuring a $5^\circ.7$ field of view. 6dF consisted of an off-telescope robotic fiber positioner, two fiber field plates of 150 fibers each (three as of 2009 February), and a bench-mounted spectrograph, mounted on the floor of the telescope dome. The spectrograph was fed from the UKST when one of the field plates was mounted to the telescope. Each fiber had a diameter corresponding to $6''.7$ on the sky and could be placed with an accuracy of $0''.7$ within the $\sim 6^\circ$ diameter field. The spectrograph used a volume phase holographic transmission grating of medium dispersing power; this $1700 \text{ lines mm}^{-1}$ grating was tuned for high efficiency in the *I*-band. This setup corresponded to an average resolving power of $R \approx 7500$ over the Ca triplet region at $8410\text{--}8795 \text{ \AA}$. The wavelength region covered by RAVE is thus very similar to that probed by the Gaia RVS instrument (Cropper et al. 2018) at somewhat lower average resolution ($R_{\text{RVS}} = 11,500$). The CCD used in the 6dF instrument was a Marconi (EEV) CCD47-BI detector that featured $13 \mu\text{m}$ pixels in a 1056×1027 array. It had a quantum efficiency of 30%–40% in the wavelength region adopted by RAVE. For further details we refer to DR1, Section 2.1.

Each field plate featured ≈ 150 fibers deployed from a ring around the periphery of the $5^\circ.7$ field. Each fiber could nominally reach 10% past the field center and was constrained to an angle of $\pm 14^\circ$, resulting in subtle allocation biases (Miszalski et al. 2006; see also Figure 3 in DR1). The actual allocatable fiber numbers typically varied between 100 and 120 (but could be as low as 80 immediately before the fiber bundles were refurbished). The most common problem for fiber unavailability was fiber breakages while parking fibers. Other problems included deterioration of fiber throughput or problems for the robot picking up fiber buttons.

Prior to configuring a field, each target was drawn from the input catalog (see Section 2.2) based on priorities given within the input target list. The targets were then manually checked for contamination, double-star proximity, and variability by downloading thumbnail images from the Supercosmos Sky Survey (SSS; Hambly et al. 2001) that were large enough to cover the fiber’s field of view. Contaminated stars were replaced until a clean, homogeneous field was achieved. Each candidate was then allocated to a given fiber using a sophisticated field configuration algorithm based on that developed for the 2dF spectrograph (Lewis et al. 2002). The field configuration algorithm accepts a user-supplied input catalog and configures fibers based on priorities given within the input target list.

Configuring a full field plate typically took about an hour, a relevant boundary condition for setting the typical exposure time (and magnitude of the targets). At a magnitude of $I = 10\text{--}11$, the exposure time to reach $S/N > 40$, the target

density of objects of that magnitude at the Galactic poles within a $5^\circ.7$ field, and the configuration time fitted neatly together to give a sensible exposure time of $\approx 1 \text{ hr}$.

After the conclusion of the RAVE survey in 2013 April, the 6dF facility (spectrograph, robot, and positioner) was decommissioned and taken out of operation.

2.2. Survey Design and Input Catalog

RAVE was designed to be a magnitude-limited spectroscopic survey that avoids any kinematic biases in the target selection. The magnitude range probed corresponds to $9 < I < 12$, where *I* is Cousins *I*. No color selection was performed (see, however, the discussion below for the added fields at low Galactic latitudes). The wavelength range of RAVE of $8410\text{--}8795 \text{ \AA}$ overlaps with the photometric Cousins *I* band.

When the RAVE survey started preparation for the first years of operation in 2002, neither the 2MASS (Skrutskie et al. 2006) nor the DENIS (Epchtein et al. 1997) catalog was available. Therefore, RAVE targets stars were drawn from the Tycho-2 catalog (Høg et al. 2000) and from the SSS. For the Tycho *I*-band, the magnitudes were estimated using the transformation formulae from ESA (1997) and Bessell (1979). The photographic I_{IVN} magnitudes in the SSS are directly equivalent to Cousins *I* (Blair & Gilmore 1982) and no further transformation was applied.

Stars between $11 < I < 12$ were exclusively drawn from the SSS. Stars with $9 < I < 11$ originated predominantly in Tycho-2, but SSS stars that did not appear within $6''.7$ (corresponding to the size of a fiber on the sky) of a Tycho star were included as well. We also did not include stars in Tycho 2 or the SSS that were within $6''.7$ of another Tycho-2/SSS star to exclude possible contamination by unresolved multiple sources. For the same reason, i.e., to avoid unresolved multiple sources within a single fiber, the initial input catalog was limited to fields at Galactic latitudes of $b > 25^\circ$, but for observing efficiency reasons (available sky regions observable with UKST for given observing epoch), fields with $15^\circ < |b| \leq 25^\circ$ were subsequently added for all Galactic longitudes (ℓ). The field centers of the first input catalog were 6° apart.

The early input catalog of the first 2 years of operation thus contained about 300,000 stars of which about half the sample originated from Tycho 2, the other half from the SSS. The first three data releases of RAVE (DR1, DR2, and DR3) are entirely based on this input catalog. An a posteriori comparison with DENIS DR3 (DENIS Consortium 2005) revealed that, owing to saturation effects for $I < 13$, a ≈ 1 mag offset between DENIS and the SSS at $I \approx 11$ emerged. As a consequence, while RAVE comprises a kinematically unbiased sample, the early input catalog exhibits some color biases (see the discussion in DR1 Section 2.3).

A new and more refined input catalog was brought into use in 2006 March. The main sample has $|b| > 25$, and uses DENIS DR3 cross-matched with 2MASS to define targets to $I = 12$ with a default of four pointings on each field center—two bright and two faint. The field centers are now 5° apart to ensure some overlap between adjacent fields. With the new input catalog, an attempt was made to more carefully extend the input catalog to lower Galactic latitudes, i.e., to include more of the Galactic disk toward the Galactic anti-rotation direction ($225^\circ < \ell < 315^\circ$, $5^\circ < |b| < 25^\circ$). A mild color cut of $J - K > 0.5$ was used in this region to avoid observing

young stars, as the weak Paschen lines in the CaT region mean that RVs and, in particular, stellar parameters, can be only poorly determined (see Section 3.3 and Figure 6 below).

In the post-2010 operations, the input catalog was further extended, again for reasons of observing efficiency, to lower Galactic latitudes and thus closer to the Galactic mid-plane, so that reddening had to be taken into account. The aforementioned color cut of $J - K > 0.5$ is capable of rejecting young foreground stars provided that $E(B - V) < 0.35$ mag. Thus, low-latitude fields ($10^\circ < b < 25^\circ$) are included for $315^\circ < \ell < 330^\circ$ and $\ell < 225^\circ$, and, analogously (for $-25^\circ < b < -10^\circ$), fields with Galactic longitudes of $\ell < 225^\circ$, $\ell > 315^\circ$ and $\ell < 30^\circ$, respectively.

The fields observed at $|b| < 25^\circ$ of the old input catalog (no color cut) compared to the new input catalog (with color cut $J - K > 0.5$) can be easily identified by having an observing date ≤ 20060312 . The stars from these earlier fields are excluded from the selection function, as discussed in Section 2.6.

Finally, and again for observing efficiency reasons, targets for $0^\circ \leq \delta \leq 5^\circ$ and $0^h \leq \alpha \leq 6^h$, $7^h30^m \leq \alpha \leq 17^h$, and $19^h30^m \leq \alpha \leq 24^h$ were needed. However, no DENIS counterpart was available for targets north of $\delta = 2^\circ$. Targets were therefore defined from 2MASS, with their estimated I magnitudes derived from 2MASS J and K , following Equation (1) in DR4.

In addition to the survey fields described above, a number of targeted observations were performed that focused on a selection of open and globular clusters. These fields were acquired to allow independent checks on the RAVE stellar parameters and their errors (for details, see DR5 Section 7.1).

For details regarding the input catalogs we refer to DR1 Section 2 and to DR4 Section 2, respectively.

2.3. Observing Procedure

Observations for RAVE followed a sequence of target field exposures, arc and flat. Ne, Rb, and Hg–Cd calibration exposures were obtained for each field, together with a quartz flat field for spectrum extraction in the data reduction. Typically, one 10 s RbNe arc exposure and five 15 s fiber flats (quartz halogen) were taken before and after each field exposure series. The field exposure series themselves consisted of five consecutive exposures (see below), allowing an adequate S/N to be obtained in the summed spectra, while minimizing the risk of saturation from particularly bright stars. In the case of poor conditions or low sky transparency, additional exposures were made.

Several target fibers were reserved in order to monitor the sky for background subtraction. Each of the RAVE target frames contained spectra of at least 10 sky samples, obtained using dedicated sky fibers. These were combined and scaled in the reduction process for sky subtraction.

We used the two field plates (three field plates starting in 2009) on an alternating basis, i.e., fibers from one field plate were configured while we observed with the other field plate. So fibers from a given field plate were mounted to the spectrograph slit prior to the observation of each field. To do this the cover of the spectrograph needed to be removed, so its temperature might change abruptly. Because of the associated thermal stress we took the flatfields and neon arc lamp exposures immediately after the set of scientific exposures, i.e.,

at a time when the spectrograph was largely thermally stabilized.

Taking account of the physical transportation and exchange of the field plates, the slew time for the telescope, field acquisition, etc., an experienced observer was able to accumulate acceptable data for up to eight RAVE fields on a midwinter's night at the latitude of Siding Spring Observatory.

2.4. Major Changes in the Performance of the RAVE Survey

RAVE observations span a period of 10 years. Based on the lessons learned with early data releases, in particular DR1 and DR2, a number of procedural optimizations were introduced. Furthermore, maintenance and refurbishments of the telescope and the facility resulted in a few modifications. We summarize the most relevant ones as follows.

1. The red color of early selected targets (DR1; Steinmetz et al. 2006) and a predicted low efficiency of the spectrograph in its second order did not call initially for a blue-light blocking filter. A Schott OG530 blue-light blocking filter was, however, inserted in the collimated beam of the spectrograph on 2004 April 2, to fully suppress the contamination, visible especially on warmer targets. This allows for an unambiguous placement of the continuum level and so permits the derivation of values of stellar parameters, in addition to the RV (DR2).
2. RAVE observations were initially limited to seven nights of bright time per lunation owing to the then ongoing 6df Galaxy Redshift Survey (6dFGRS; Jones et al. 2009). With the conclusion of 6dFGRS on 2005 July 31, RAVE proceeded through the end of 2012 at an observing rate between 20 and 25 nights per lunation.
3. On 2006 March 13, the new DENIS+2MASS based input catalog was introduced (see Section 2.2 and DR4 Section 2).
4. On 2006 March 29, the number of fiber flats was increased from one to five.
5. RAVE observations initially consisted of five exposures of 600 s. Since the beginning of 2007, RAVE targets were segregated into four magnitude bins ($\text{bin}_1: 8 \leq I \leq 10$; $\text{bin}_2: 10 \leq I < 10.8$; $\text{bin}_3: 10.8 \leq I < 11.3$; $\text{bin}_4: 11.3 \leq I < 12$) in order to maximize observing efficiency and to avoid cross-talk contamination of fibers on faint sources adjacent to fibers targeting bright objects. Exposure times corresponded to 5×600 s for bin_1 and bin_2 , 5×900 s for bin_3 , and 5×1200 s for bin_4 .
6. Observations were paused between 2007 June 4 and 11 for service on the 6dF robot and between 2007 June 26 and August 6 for asbestos removal work at the UKST.
7. In 2009 February a third field plate was introduced and subsequently the original two field plates were fully refurbished with new fiber bundles. After this procedure, each observing night started with two fully configured field plates, thus considerably increasing the survey speed.
8. The Wambelong bushfire at Siding Spring in early 2013 forced observations to be suspended between 2013 January 13 and April 1.

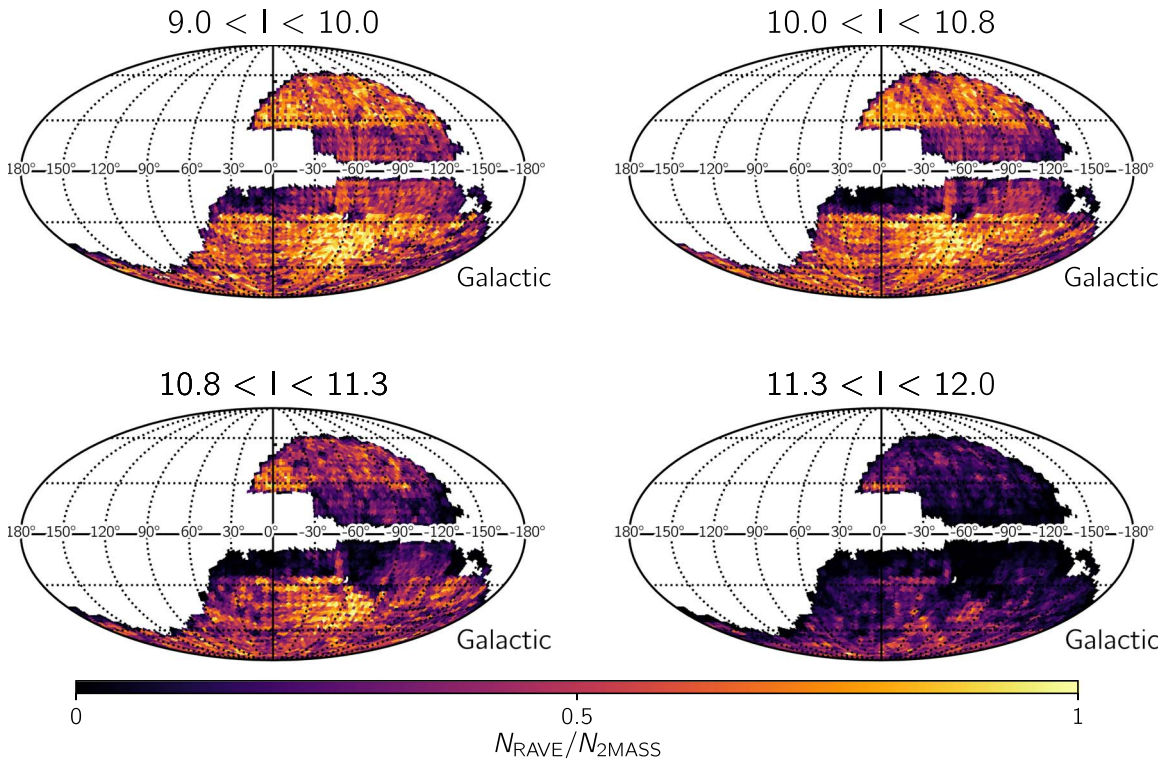


Figure 1. Mollweide projection of Galactic coordinates of the completeness of the stars for which RAVE DR6 radial velocity measurements are available for the core sample (see Section 6). Each panel shows the completeness over a different magnitude range, where the HEALPix pixels are color-coded by the fractional completeness ($N_{\text{RAVE}}/N_{2\text{MASS}}$).

2.5. Data Reduction

The data reduction of RAVE follows the sequence of the following pipeline:

1. quality control of the acquired data on site with the RAVEdr software package (Section 3.1);
2. reduction of the spectra (Section 3.1);
3. spectral classification (Section 4);
4. determination of (heliocentric) RVs with SPARV (*Spectral Parameter and Radial Velocity* (Section 5));
5. determination of atmospheric parameters with MADERA (*MATisse and DEgas used in RAve* (DR6-2, Section 3.1; see also Kordopatis et al. 2013));
6. determination of the effective temperature using additional photometric information (*InfraRed Flux Method* (DR6-2, Section 3.2; see also Kunder et al. 2017));
7. determination of atmospheric parameters combining RAVE spectroscopic information with additional photometry and Gaia DR2 parallax priors using BDASP (*Bayesian Distances Ages and Stellar Parameters* (DR6-2 Section 3.3; see also McMillan et al. 2018));
8. recalibration of the stellar parameters for giant stars based on K2 asteroseismic information (DR6-2, Section 3.4; see also Valentini et al. 2017);
9. determination of the abundance of iron group elements and an overall $[\alpha/\text{Fe}]$ ratio with the pipeline GAUGUIN (DR6-2, Section 4).

The output of these pipelines (see also Table 1) is accumulated in a PostgreSQL database and accessible via the RAVE website <http://www.rave-survey.org> (Section 7 and DR6-2, Section 7).

2.6. Survey Selection Function

In order to draw robust conclusions from the data gathered via large spectroscopic surveys such as RAVE, it is crucial to understand the relationship between the observed targets and their underlying population, known as the selection function. A comprehensive overview of the selection function of RAVE is given in Wojno et al. (2017), which we summarize here. RAVE targets were selected from a number of input catalogs. These targets were selected uniformly over the entire southern hemisphere, with the exception of regions where a mild color-cut of ($J - K > 0.5$ mag) was enforced (Section 2.2). Figure 1 shows the completeness fraction (number of RAVE stars divided by number of 2MASS stars per area on the sky) for the observed I magnitude bins. The I magnitude is in principle available from catalogs as DENIS; however, DENIS I suffers from saturation effects for $I < 10$. As in Wojno et al. (2017), we approximate the DENIS I magnitude from 2MASS J and K_s via

$$(I - J) = (J - K_s) + 0.2 \exp \frac{(J - K_s) - 1.2}{0.2} + 0.12 \quad (1)$$

(for the number of spectra based on measured APASS i' magnitude (for RAVE DR4), see Figure 11 of Munari et al. 2014). Figure 2 shows the completeness of stars with determined RVs over the overall RAVE footprint. As Wojno et al. (2017) showed for RAVE DR5, we also find RAVE DR6 to be kinematically unbiased.

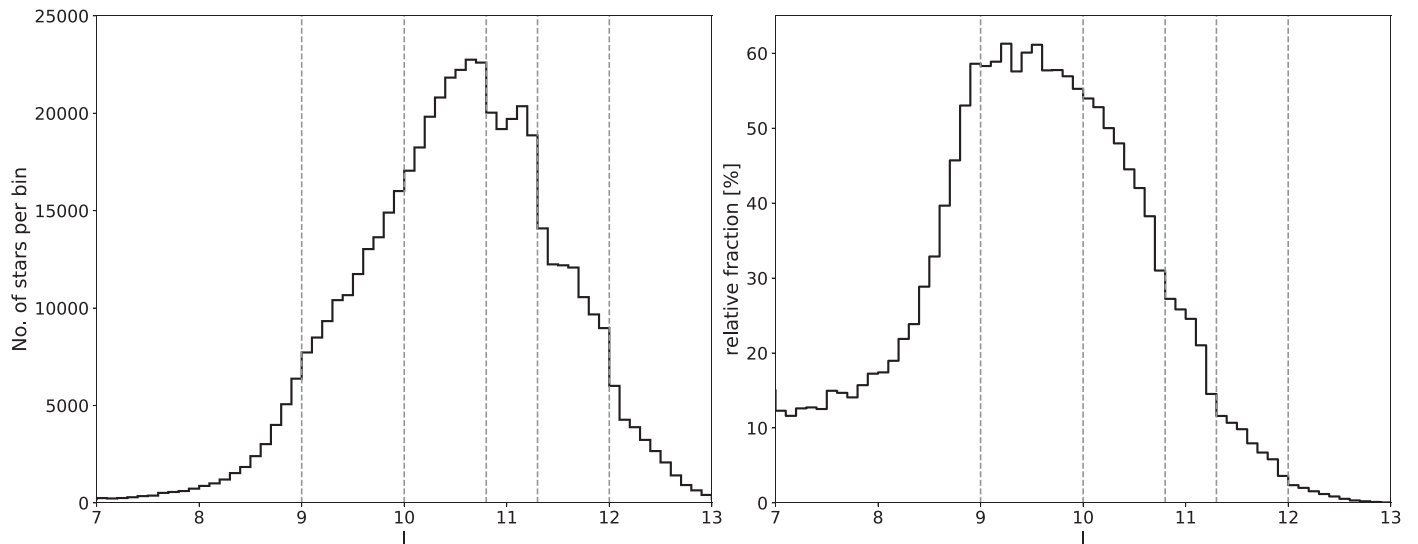


Figure 2. Left: histogram of the number of spectra with derived radial velocities (RVs) in the RAVE footprint per I magnitude bin of 0.1. Magnitude bins used per field plate are indicated with dashed lines (see Section 2.2). Right: completeness of RAVE DR6 (stars with RVs) with respect to the completeness of 2MASS is shown as a function of I magnitude.

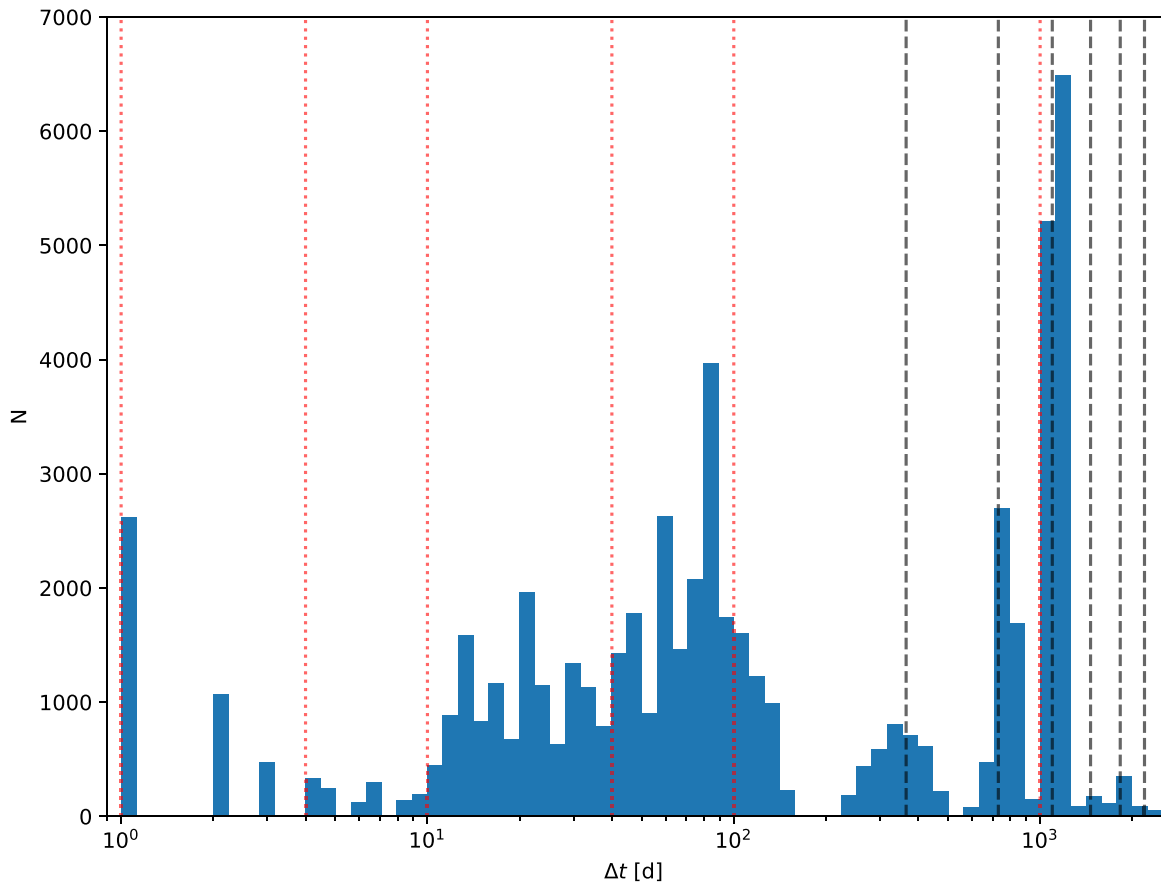


Figure 3. Time interval between consecutive observations of stars with at least four repeat observations. The red dotted lines mark the guiding cadence of 1, 4, 10, 40, 100, and 1000 days, the black dashed line multiples of 365 days.

2.7. Repeats

RAVE was designed as a survey with its main focus on studies of Galactic dynamics and Galactic evolution. The primary design goals were therefore to have an unbiased input catalog and observing procedure, a wide coverage of the accessible sky, and a

magnitude-limited layout aiming at high completeness from the brighter to the fainter magnitudes. The technical boundaries (large multiplex and long configuration times combined with weather patterns and block-out periods around the full Moon) made it difficult to account systematically for repeat observations

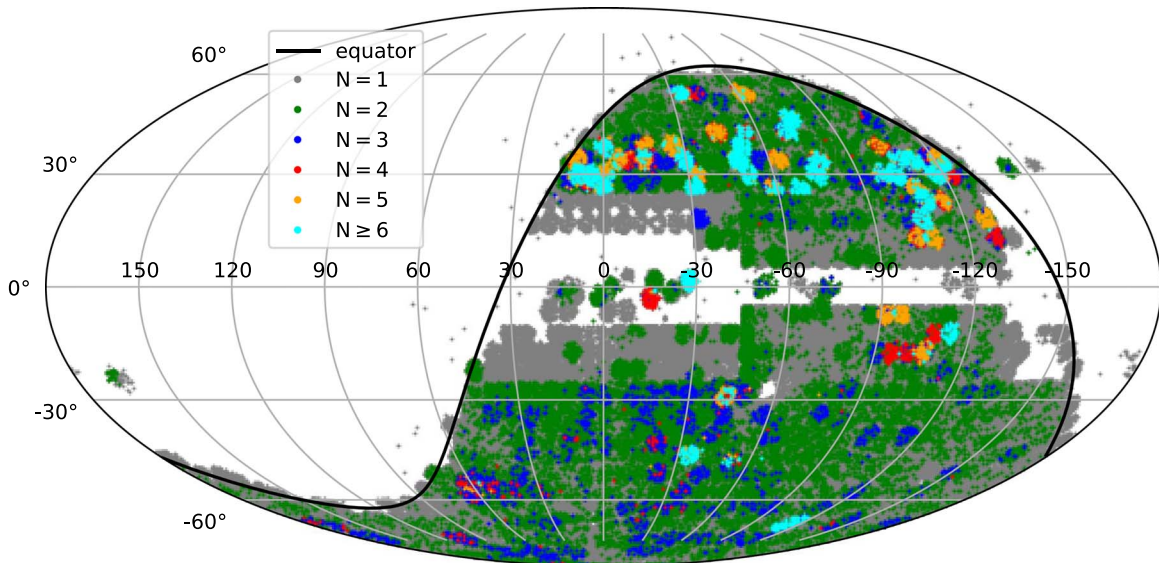


Figure 4. Mollweide projection of RAVE fields color-coded by the number of revisits.

Table 1
Contents of RAVE DR6

in DR6	No. of Spectra	No. of Unique Stars
Observed targets	518,387	451,783
–with $\text{snr_med_sparv} > 20$	474,649	416,365
–with $\text{snr_med_sparv} > 40$	262,199	232,282
–with $\text{snr_med_sparv} > 60$	66,815	58,992
–with $\text{snr_med_sparv} > 80$	14,056	12,417
with 2MASS cross match	518,300	451,706
with Gaia DR2 cross match	517,095	450,641

Table 2
Stars with Multiple Observations in RAVE DR6

	in DR6
Stars with one visit	404,428
Stars with two visits	39,340
Stars with three visits	3606
Stars with four visits	1034
Stars with five visits	1418
Stars with six visits	1205
Stars with seven or more visits	757

following a fixed cadence, in particular without compromising the aims of coverage and completeness. On the other hand, repeat observations are critical to check for coherency and repeatability of RAVE data products, and to allow modelers to account for the effects of unresolved binaries.

In order to measure, at least statistically, the effects of binarity, about 4000 stars were selected for a series of repeat observations in the observing semester 2009A (2009 February 1–July 31). The aim was to roughly follow a logarithmic series with a cadence of separations of 1, 4, 10, 40, 100, and 1000 days. The repeat sequence was selected from the first observations of the new input catalog introduced on 2006 March 12, so the difference between the 2009 and the 2006 observations served to approximate the 1000 day separation. Weather patterns, block out periods, and fiber availability, however, resulted in considerable dispersion and non-observations around the target cadence (Figure 3). The repeat sequence mainly constitutes the subsets with four, five, six, and more than seven observations (see Table 2), and can clearly be seen in the clustering at $-120^\circ < l < 30^\circ$ and $b > +30^\circ$ (Figure 4).

In addition to these systematic repeats, whole fields were repeated when they were marked as problematic in the post-observation quality review. Furthermore, individual stars could be re-targeted if no higher-priority (i.e., unobserved) targets were available in the fiber configuration process. These quality repeats and chance repeats make up most of the targets with two or three visits. Indeed, Figure 4 reveals that these targets

are much more evenly spread over the RAVE footprint, as expected. Finally, targeted observations of calibration fields, in particular open and globular clusters, also give rise to many repeat observations, also visible in the Mollweide projection of Figure 4.

3. RAVE Spectra

3.1. Spectra and Their Reduction

All RAVE spectra were reduced with a semi-automated pipeline based on a sequence of dedicated IRAF routines. The use of a pipeline approach ensures a proper uniformity of reductions, while the requirement of specific human-approved standardized checks increases their reliability. The pipeline is described in DR1 and DR2. Here we summarize its main features and report on experience gained over a decade of its use. We also add specific information that is relevant for legacy purposes and is important for readers who would like to understand the underlying systematics.

To account for the temperature sensitivity of the spectrograph (Section 2.3), we adopted a policy where each set of scientific exposures was accompanied by a flat-field and an arc-line exposure, both usually done immediately after the scientific ones. Flat-field exposures were used to establish the position, width, and shape of spectral tracings in other exposures, to normalize relative fiber throughput, and to filter out interference fringing, which can be quite prominent when

Table 3
Wavelengths of Arc Lines

Element	Wavelength (Å)
Ar I	8408.2096
Ar I	8424.6475
Ne I	8495.3598
Ar I	8521.4422
Ne I	8591.2583
Ne I	8634.647
Ne I	8654.3831
Ne I	8780.621
Ne I	8783.7533

using a thinned backside-illuminated CCD detector at the RAVE wavelength range. Typically, fringing jumps that reach up to 20% of the flux are damped to $\sim 1\%$ with this approach, but note that techniques of Gaussian filtering would be required to reach a better continuum normalization on scales of ~ 20 Å, a typical fringe width. A small fraction of RAVE spectra suffer from internal reflection of light within the spectrograph, which causes an emission ghost located blueward of the Ca II 8498 Å line. This is an additive feature that can be removed through careful spectral normalization, though its width of ~ 23 Å makes this a challenging task. Such spectra have a problematic continuum, so they are flagged with “c” (Table 4) in the final database.

Extracted one-dimensional spectra of object, flat-field, and arc-lamp exposures need to be corrected for fiber cross-talk and for scattered light contributions from all fibers with flux levels above a set threshold. Fiber cross-talk is removed iteratively, assuming a Gaussian shape of fiber illumination in the direction perpendicular to the tracing direction. In the end, we estimate that in the final spectrum the contribution of stars to adjacent fibers does not exceed 0.001 of their flux. About 13% of the incoming light is scattered in the spectrograph, with the exact amount decided manually by minimizing the flux in the gaps between the three fiber sub-bundles (fibers 50–51 and 100–101) and by analyzing flux levels in sky fibers that have very low continuum levels or, in the case of cirrus clouds and moonlight, should have positive fluxes compatible with the strength of the solar spectrum in lines of the infrared Ca triplet. In our model the scattered light from each point in the focal plane is scattered over an axially symmetric Gaussian with a FWHM of ~ 200 CCD pixels.

A neon arc lamp exposure is used to wavelength calibrate the spectra. The lamp includes nine emission lines in the RAVE spectral range that are strong enough for this purpose. Table 3 reports their adopted wavelengths. Note that each spectrum includes 1031 pixels spanning a wavelength range of 384.6 ± 1.7 Å, but its central wavelength varies in a parabolic manner from ~ 8595 Å at the edges of the field plate to ~ 8604 Å at its center (see Figure 3 in DR2). Consequently, the Ar I 8408 Å arc line is missing in fibers near the center of the field plate while at the edges of the field plate extrapolation has to be used to wavelength calibrate the reddest 15 Å of the wavelength range. All observed spectra have been fit using five or more arc lines and 91% have been fit using $N = 8$ arc lines. A single cubic spline with $df = 4$ free coefficients is used to convert pixel units into wavelengths. Per line it achieves a median difference between the fitted and assumed wavelength of 0.015 Å (for 99% of the spectra, this difference is smaller than 0.072 Å), which at 8600 Å corresponds to 0.52 km s^{-1} .

This implies a typical error in the derived RV of $\sim 0.52/\sqrt{N - df} \text{ km s}^{-1} = 0.26 \text{ km s}^{-1}$. So the RV accuracy is mostly limited by temperature shifts in the spectrograph, by the achieved S/N, and by the accuracy of flat-fielding, and not by uncertainties in the wavelength calibration.

In 90% of cases the spectra of sky fibers are dominated by sky emission lines and have negligible continuum levels, while the rest include a detectable level of moonlight, usually scattered on thin cirrus clouds. The main contributors to sky spectra are therefore airglow emission lines belonging to three series: OH transitions 6–2 at wavelengths shortward of 8651 Å, OH transitions 7–3 at wavelengths longward of 8758 Å, and O₂ bands between 8610 and 8710 Å (see DR5 for details). Both airglow and cirrus scattering can vary on shorter timescales and smaller spatial scales than a typical ~ 50 min sequence of scientific exposures over a $5^\circ.7$ field of view. Therefore, we assume a complete scrambling and use a scaled median of sky fibers as the background model. The user should be aware that in rare cases this may not be true, as both airglow line intensity and cirrus cloud scattering may depend on fiber position. In such cases objects with adjacent positions on the sky should show similar levels of sky residuals. We made sure that to the best of our knowledge the sky fibers were positioned on “empty” regions of the sky. We used two additional checks to avoid sky over-subtraction due to contamination by unknown sources: first, the person responsible is asked to visually approve all sky spectra to be used in the background calculation and, second, the use of a scaled median rejects any remaining outliers.

Airglow emission lines have fixed wavelengths, so they have been used for the calculation of the RV zero-point and for the correction of temperature fluctuations in the spectrograph. Their signal is much cleaner in the sky fibers than in the stellar spectra. The zero-point correction is obtained from a weighted sum measurement of sky and stellar spectra, with the former having a 10-times higher weight and typically amounts to $\approx -0.5 \pm 1 \text{ km s}^{-1}$.

The final stages of reduction include sky subtraction and shifting of the stellar spectrum to the inertial frame of the solar system barycenter. Note that at all stages of the reduction the wavelength bin corresponds to one pixel in the dispersion direction. This simplifies the recognition and treatment of discrete features, like cosmetic defects of the CCD or cosmic ray hits. A sequence of five 10 minute exposures of each object is median-combined, thus rejecting most of the cosmic ray hits (except for the rare hits in the flat-field exposure).

As a final check, the pipeline makes two graphs that are visually inspected and stored: the first plot compares measured average fluxes in individual fibers with those expected from the available ground-based photometry. Since fiber throughput varies over time and position, we advise the user to use normalized spectra only. Still, a comparison of fluxes should show a clear correspondence with stellar magnitudes and low or negligible fluxes in sky and parked fibers. This helps to avoid any book-keeping errors, which are always possible when observing hundreds of thousands of stars over thousands of nights. Finally, the responsible person is shown a collection of final spectral tracings of a given field: the idea is to check that the results seem reasonable, but a visual check of every spectrum is not feasible for such a large survey. The design of the spectrograph does not allow one to derive accurate absolute fluxes, so we provide spectra with a normalized continuum.

These are derived with an iterative low-order polynomial fitting and with asymmetric rejection limits. We use a second-order spline function with the upper rejection limit set to two residual standard deviations and lower limit to 1.3. Note, however, that any comparison of observed and synthetic spectra requires that *both* spectra be first normalized *again* using the same normalization parameters.

In summary, RAVE uses a dedicated data reduction pipeline, which has been tuned by our experience gained over a decade of its use. Our insistence on specific human-approved checks and adjustments increases the reliability of its results. Note that this is different from surveys that use general-purpose instruments and often use or at least start with the instrument-supplied pipeline. On the other hand, the HERMES spectrograph is a general-purpose instrument at the AAO, but its extensive use by the GALAH survey makes the survey’s dedicated pipeline (Kos et al. 2017) increasingly popular also for general users as well. Finally, we note that all these pipelines use the standard reverse-modeling approach. It seems that with photonic combs an alternative forward-modeling approach is possible, which convolves a list of spectral templates with assumed values of stellar parameters with known aberrations in the spectrograph to produce a fit to the original CCD image. This approach may yield much better results in the future (Kos et al. 2018).

The wavelength range of the RAVE spectra is dominated by strong spectral lines: for the majority of stars, the dominant absorption features are due to the infrared Ca triplet, which in hot stars gives way to the Paschen series of hydrogen. There are also weaker metallic lines present for solar-type stars and molecular bands for the coolest stars. Within an absorption trough the flux is small, so shot noise is more significant in the middle of a line than in the adjacent continuum. Error levels also increase at wavelengths of airglow sky emission lines, which have to be subtracted during reduction. As a consequence, a single number, usually reported as S/N, is not an adequate quantification of the observational errors associated with a given spectrum. For this reason, we provide error spectra that comprise uncertainties (“errors”) for each pixel of the spectrum. These are provided both for spectra prior to sky subtraction and for the final sky-subtracted ones (for details, see DR5, Section 4).

The main contribution to the error spectrum is shot noise, which can be parameterized as $S/N = gN_s/\sqrt{gN_u}$, where N_u is the number of counts per pixel before sky subtraction, N_s is its counterpart after the subtraction, and the effective gain $g = 0.416 \text{ e}^-/\text{ADU}$ (see DR5 for details). As explained above, the main source of the difference between N_u and N_s is airglow emission lines. So the relative flux errors increase within deep stellar absorption lines, such as the Ca II infrared triplet, and at positions of airglow lines. Note that subtraction of the latter in the sky-subtracted spectra may be sub-optimal due to a rapid variability of sky airglow. Other contributions to the error spectrum are scattered light and imperfect flat-field fringing removal, which typically contribute at a 0.8% level, added in quadrature. Finally, the resulting error spectra are smoothed with a window of a width equal to 3 pixels in the dispersion direction, which takes into account the noise correlation between adjacent pixels.

Error spectra are given as relative errors. A value of 0.01 implies that a 1% error in flux with an expected approximately Gaussian distribution at this wavelength bin.

3.2. Signal-to-noise Ratio

As described in the previous paragraph, the errors on the normalized fluxes of the reduced spectra vary from pixel to pixel and it is problematic to represent a whole spectrum with a single value. On the other hand, a priori estimates of the S/N per pixel are needed for the RV and stellar-parameter pipelines (see, e.g., DR2, Section 3.4, DR3 Section 2.2, or DR4, Section 3.2). The corresponding values are reported in the respective catalog files (Section 7 and DR6-2, Section 7).

A better a posteriori estimate describing the quality of a spectrum, e.g., for data selection for a particular science application, is given by `snr_med_sparv`, defined as the inverse of the median of the error spectrum. `snr_med_sparv` scales on average with `snr_sparv` in a somewhat stronger than proportional manner (see Figure 5). The median `snr_med_sparv` over the whole SPARV sample is ≈ 40 (see Figure 5).

3.3. Morphology of RAVE Spectra

A sample of typical RAVE spectra and their associated error spectra for a range of targets is shown in Figure 6. In all spectra other than those for the hot dwarf and the cool star with molecular bands, the Ca triplet can easily be recognized as the dominant feature. For hot dwarfs, the Ca triplet feature is replaced by strong and broad Paschen lines. Consequently, RVs can only be determined poorly for this class of stars, and atmospheric parameters (if at all convergent) are highly unreliable. The Ca triplet wavelength region also shows a considerable number of weak metal lines, which are used in Section 4 of paper DR6-2 to derive abundances of individual elements and $[\alpha/\text{Fe}]$ -ratios. These absorption lines are clearly visible in the high signal to noise cases and also in the moderate-S/N spectrum 6), but become difficult to discriminate against noise for S/N of 20 and lower, as we demonstrate more quantitatively in Section 6 of paper DR6-2.

4. Spectral Classification

The classification of RAVE spectra was introduced in Matijević et al. (2012). For this data release we modified the original classification scheme in order to simplify its use. Previously, the classification of RAVE spectra was given as a series of 20 flags for each spectrum. These flags represented the 20 nearest neighbors in the locally linear embedding projected space and were ordered according to (decreasing) relative weights. In the revised version we first re-normalize all 20 weights so they sum to unity and then add all weights belonging to each flag. For example, in the case of a spectrum that has 13 normal star flags, six chromospherically active star flags and one binary star flag, we add 13 re-normalized weights for the normal stars and so on for the rest. This results in only three flags (for the flags and their occurrence see Table 4) plus their respective weights and enables the user to choose quantitatively among the morphological types of spectra. It should be noted that the summed weights are not equal to the probability that a spectrum belongs to a certain class but can be used as a proxy. In many cases all 20 original flags are of the same class so we only report a single flag with a single summed weight of 1.0. In cases where there are more than three different classes assigned to a single spectrum we report the first three, with the highest summed weights in decreasing order (the first one always being the largest). Consequently, the sum of the

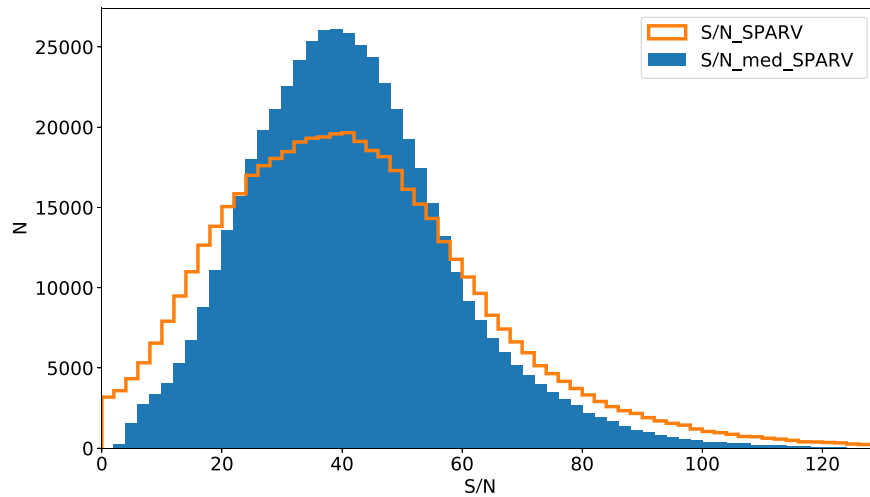


Figure 5. Distribution of the a posteriori signal-to-noise estimate `snr_med_sparv` and the a priori estimates `snr_sparv` for all stellar spectra in the RAVE DR6 database.

three weights w_1 , w_2 , and w_3 is less than or equal to one. Of the 518,392 spectra in this release 490,959 (94.7%) have the first of the flags with the value “n,” i.e., they are classified as likely to be normal stars.

We can both illustrate and verify the automated classification scheme by showing where stars of different classification lie in the $\log g$ versus T_{eff} plane (Kiel diagram, Figure 7): The classification scheme clearly shows the transition to hot stars above a temperature of $T_{\text{eff}} \approx 7000$ K owing to the presence of strong Paschen line features, which dominate over the Ca triplet feature. On the main sequence, at effective temperatures below 5000 K, chromospheric emission lines become more prevalent in these cool and active stars (Žerjal et al. 2013). At temperatures below 4000 K, molecular lines lead to a classification of the star as cool or as having carbon features, in particular near the tip of the giant branch. A slightly pinkish color in the sequence parallel to the main sequence for temperatures above 4500 K also indicates a binary origin of stars in this part of the $\log g$ versus T_{eff} plane; for temperatures below 4500 K, the emission-line characteristics dominate the classification also in this part of the parallel sequence.

5. Radial Velocities

RVs are derived with the pipeline `SPARV` in a manner identical to that presented in DR4 and DR5, and as detailed in Section 2 of DR3. The spectra are cleaned in the spectral regions that are strongly affected by fringing (DR3 Section 2.4) and then matched to a grid of spectra discretized in T_{eff} , $\log g$, $[M/H]$, $[\alpha/Fe]$, and stellar rotational velocity v_{rot} , assuming a fixed microturbulence $\xi = 2 \text{ km s}^{-1}$. The underlying algorithm is a standard cross-correlation algorithm in Fourier space. The grid employs the synthetic spectral library of Munari et al. (2005) based on ATLAS 9 model atmospheres, and was extended with a finer grained spacing toward the densest region of the observed parameter space. The grid has $[M/H] = -2.5, -2.0, -1.5, -1.0, -0.8, -0.6, -0.4, -0.2, 0.0, 0.2, 0.4, \text{ and } 0.5$ dex. For stars cooler than 4500 K the grid includes also molecular lines, while any influence of dust or chromospheric activity is neglected. The latter can be important in young cool stars descending toward the main sequence (Žerjal et al. 2013, 2017), so an increased template mismatch reflects

in an increased RV error for such objects. The process to match templates and thus derive RVs follows a two-step procedure. In a first step a provisional estimate of the RV is obtained using a subset of only 10 template spectra. This first estimate typically results in RVs with an accuracy better than 5 km s^{-1} and is used to put the spectrum in the zero-velocity frame. Then a new template is created using a penalized chi-square method as described in DR2, which in turn is used to derive the final, more precise RV. To determine the zero-point, the processing pipeline uses the available sky lines in the RAVE wavelength window and fits a combination of a third-order polynomial and a constant function to the relation between sky RV and fiber number (see DR3 Section 2.5). This fitting function defines the mean trend of zero-point offsets and provides the zero-point correction as a function of fiber number. The internal error is defined as the error in the determination of the maximum of the correlation function using IRAF `xcsao`. This procedure results in RVs with an internal error distribution peaking near 1 km s^{-1} with a long tail toward higher RV errors probably owing to problematic spectra and/or variability from stellar binaries (see Figure 8); 68% of the sample has an internal accuracy better than 1.4 km s^{-1} (see DR5).

The RVs and their respective errors are confirmed by external observations and also by those targets that have repeat observations (see DR4 and DR5). The long tail in the repeat observations can be reduced by 90% by applying quality criteria indicative of derived RVs with high confidence, namely $|\text{correctionRV}| < 10 \text{ km s}^{-1}$, $\sigma(\text{RV}) < 8 \text{ km s}^{-1}$, and $\text{correlationCoeff} > 10$ (Kordopatis et al. 2013).

RVs provided by RAVE do not include corrections for gravitational redshift effects, nor do they take into account any convective motions in the stellar atmosphere. As discussed in DR2, our choice to omit these two contributions follows Resolution C1 of the IAU General Assembly in Manchester (Rickman 2001) and is consistent with the derived RVs reported by most other spectroscopic surveys, including Gaia DR2. The reader should, however, note that such an RV does not correspond to the line-of-sight component of the velocity of the stellar center of mass, which corresponds to the RV reported by the GALAH survey (Zwitter et al. 2018) and which is expected to be followed also by Gaia DR3. Typical values of gravitational redshifts are $+0.5 \pm 0.2 \text{ km s}^{-1}$ for dwarfs and

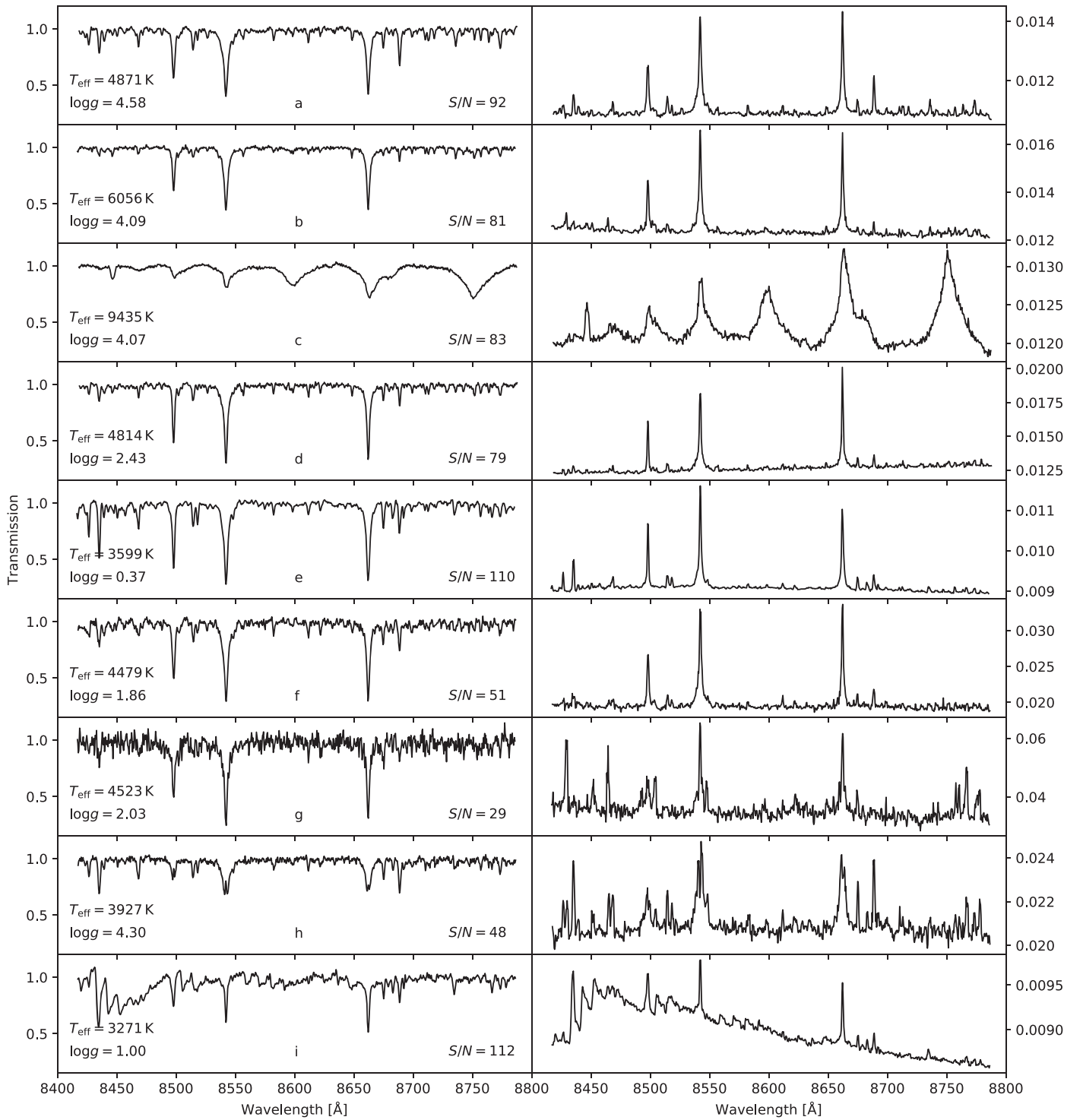


Figure 6. Typical spectra (left) and error spectra (right) for some typical objects in the RAVE database. Stellar parameters are derived using the BDASP pipeline (see DR6-2, Section 3.3). From top to bottom: (a) a high-S/N cool dwarf; (b) a high-S/N warm dwarf; (c) a high-S/N hot dwarf; (d) a high-S/N red clump star; (e) a high-S/N giant star; (f) a moderately high-S/N giant; (g) a low-S/N giant; (h) an emission-line cool dwarf; (i) a very cool star with molecular bands (using calibrated stellar parameters obtained via the MADERA pipeline (see DR6-2, Section 3.1)). Error spectra are given as relative errors. A value of 0.01 implies that a 1% error in flux with an approximately Gaussian distribution is expected at this wavelength bin.

$+0.1 \pm 0.1 \text{ km s}^{-1}$ for giants, while convective shifts in the optical range are $-0.45 \pm 0.15 \text{ km s}^{-1}$ for dwarfs and $-0.3 \pm 0.2 \text{ km s}^{-1}$ for giants (Zwitter et al. 2018). As these values do not cancel exactly one should take care when studying the detailed internal dynamics of loosely bound stellar associations or streams where the reported RAVE RVs may

exhibit systematic effects with spectral type at a level of $\sim 0.1 \text{ km s}^{-1}$.

6. Validation of RAVE DR6 Parameters

The data product of large surveys like RAVE is always a compromise between the quality of the individual data entry and

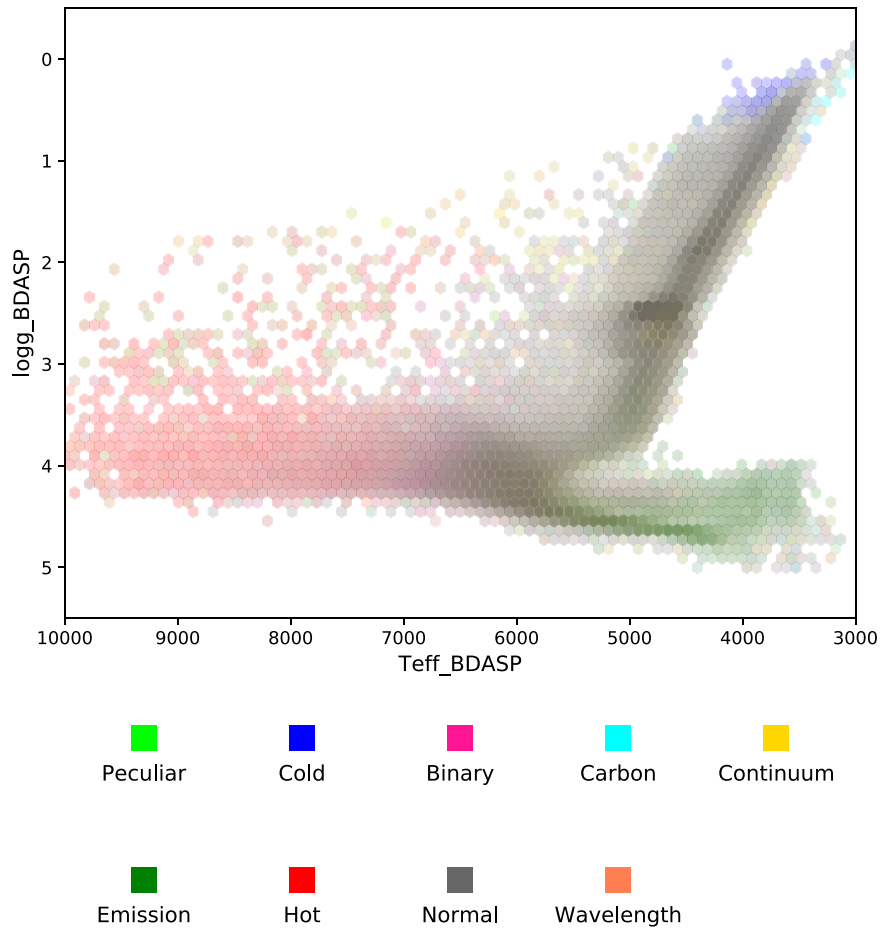


Figure 7. Kiel diagrams assuming: T_{eff} and $\log g$ from the BDASP pipeline (see DR6-2), color encoded by the average automated classification of the stars in the respective hexagon.

Table 4

Description of the Classification Flags as Described in the Respective Section of Matijević et al. (2012)

Label	Description	N_{flag1}	Comment
n	normal stars	490,955	Section 4.1
o	hot stars ($T_{\text{eff}} > 7000$ K)	5410	Section 4.1
b	binary stars	3123	Section 4.2
d	cool dwarfs	181	Section 4.3
e	chromospheric emission lines/active stars	6345	Section 4.3
t	TiO band stars/cool giants	5297	Section 4.4
g	cool giants	69	Section 4.5
h	hot giants	51	Section 4.5
a	carbon stars	271	Section 4.6
p	peculiar stars	82	Section 4.7
c, w	problematic spectra	6603	Section 4.8

the area and depth of the survey. This applies to design decisions (like the applied exposure time/targeted S/N) as well as to the decision of which data to keep in the sample and which ones to exclude. Our policy for RAVE is to provide the maximum reasonable data volume possible, which allows the user to consider the tails of the distribution function. *The exact choice of the (sub)sample used for a particular science case has to be made by the user based on the criteria needed for the respective science application!* Here, we only can give some first guidelines/recommendations regarding the data downselection.

Table 5

RAVE Subsamples Used in this Publication for Validation and First Science Applications

Sample	Selection Criteria	Sample Size	Unique Objects
RV00	$\text{correlation}_{\text{coeff}} > 10$	497,828	436,340
RV20	RV and $\text{snr}_{\text{med_sparv}} > 20$	468,238	411,761
RV40	RV and $\text{snr}_{\text{med_sparv}} > 40$	259,316	230,126
RV60	RV and $\text{snr}_{\text{med_sparv}} > 60$	65,410	57,783
RV80	RV and $\text{snr}_{\text{med_sparv}} > 80$	13,528	11,922

For a description of the various parameters in the following paragraph, we refer to the tables in Section 7.

Stars with $\text{correlation}_{\text{coeff}} > 10$ have an internal velocity error distribution that peaks near $\varepsilon_{\text{HRV}} \approx 1\text{--}2$ km s⁻¹ with the tail toward very large velocity errors strongly suppressed compared to the uncut sample (see Figure 8). For repeat measurements, such a sample features a small scatter in the repeat measurements of their heliocentric RV. The distribution peaks near 0.0 km s⁻¹, and the tail toward very large velocity differences is reduced by 90%, again compared to the uncut sample, indicative of a high-confidence measurement (see below). We refer to the data set defined by these criteria as the core sample, or RV00.

The reported internal RV errors reflect both statistical uncertainty and systematics owing to a mismatch between

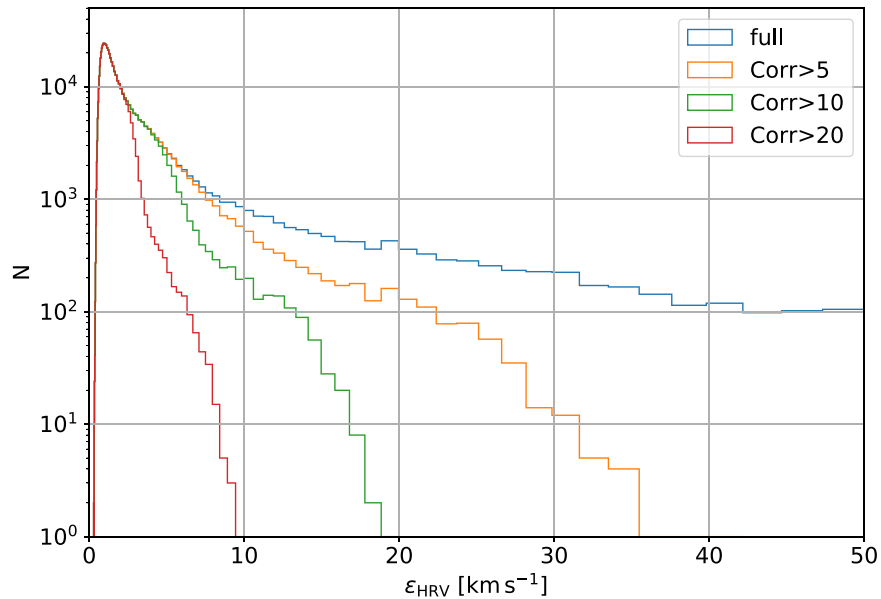


Figure 8. Distribution of the internal error estimate ϵ_{HRV} for the full sample and for subsamples with a correlation coefficient R larger than 5, 10, and 20, respectively. Increasing the requirements on R strongly suppresses the tail of high-velocity errors.

observed and synthetic spectra. The RAVE RVs and their uncertainties can be verified against independent external sources (Section 6.1), providing a measure for the accuracy, or internally by considering repeat observations providing an estimate of the precision (Section 6.2).

We alert the reader that the above-mentioned quality criteria were drawn under the assumption that RAVE is used as a statistical sample. Should the RAVE catalogs be used to identify individual candidates for follow-up studies (e.g., candidates for high RVs), additional criteria constraining the uncertainty of the measurement $\sigma(\text{RV})$ and of the zero-point correction (`correction_rv`) should be applied.

6.1. Validation of RVs against Gaia DR2

The accuracy of RAVE RVs as compared to external observations was extensively discussed in DR3 Section 3.1 and DR4 Section 8.1. On 2018 April 25, the second data release of the ESA mission Gaia was published (Gaia Collaboration et al. 2018), featuring RVs for some 7 million targets. The Radial Velocity Spectrometer (RVS) of Gaia also operates in the Ca triplet region, though at a somewhat higher resolution of $R = 11,000$. The RVs of RAVE DR5 and Gaia DR2 are compared in Steinmetz et al. (2018), showing a very good agreement between both data sets and also identifying a very small subset of RAVE stars in DR5 with problematic wavelength calibration (almost exclusively stars at the edge of the field plate at observing periods with a high rate of disabled fibers). These stars have been removed in DR6 (see the Appendix). RAVE DR6 and Gaia DR2 have 450,646 stars in common. This provides an opportunity to comprehensively compare RAVE and Gaia RVs. Since RAVE, however, provided the largest subset of targets for validating the Gaia pipeline (Sartoretti et al. 2018), the two data sets are not fully independent. Furthermore, the RVS of Gaia covers the same spectral range at a similar resolving power, so that any spectral mismatches approximately cancel each other out.

Figure 9 compares the RVs published in Gaia DR2 with those presented here (RV00 sample). Overall this comparison confirms the excellent agreement between those two data sets. The velocity differences can well be matched with two Gaussians with standard deviations of 1.2 km s^{-1} and 3.4 km s^{-1} , respectively, plus an additional exponential tail toward higher velocity errors. We will discuss the possible origins of this behavior in the next section.

There is a systematic offset of about -0.32 km s^{-1} . The offset is also comparable to the offset found between Gaia DR2 and other ground-based spectroscopic surveys in a similar magnitude range, such as APOGEE (Sartoretti et al. 2018), indicative that the source for this offset may at least partially be related to the RV zero-point of Gaia DR2. The difference is also within the internal error estimates described above, errors as compared to external samples, and errors derived from a subset of stars with repeat observations.

A further analysis exhibits no systematic tendency of the RVs with RAVE-derived effective temperatures for stars with $4000 \text{ K} < T_{\text{eff}} < 7000 \text{ K}$ (Figure 10, left panel). Stars cooler than 4000 K exhibit a somewhat smaller shift of -0.1 km s^{-1} . For stars hotter than 7000 K (a small subset of the RAVE sample), the accuracy of the RV deteriorates, resulting in a larger systematic shift and a considerably increased spread, owing to the increasing dominance of broad Paschen lines at the expense of a less prominent Ca triplet. With increasing S/N, the prominence of the 1.2 km s^{-1} Gaussian increases, while that of the 3.4 km s^{-1} Gaussian decreases. A lower fraction of dwarf stars ($\log g > 3.5$) lies within the 1.1 km s^{-1} Gaussian than for giant stars (Figure 10, middle panel).

There is a very mild tendency for the velocity shift between RAVE and Gaia DR2 to change with metallicity (Figure 10, right panel). This effect amounts to about 0.5 km s^{-1} between $[\text{Fe}/\text{H}] < -1$ and $[\text{Fe}/\text{H}] > 0$.

6.2. Validation with Repeat Observations

A further way to validate the quality of the RAVE data products is to compare the parameters derived for multiple

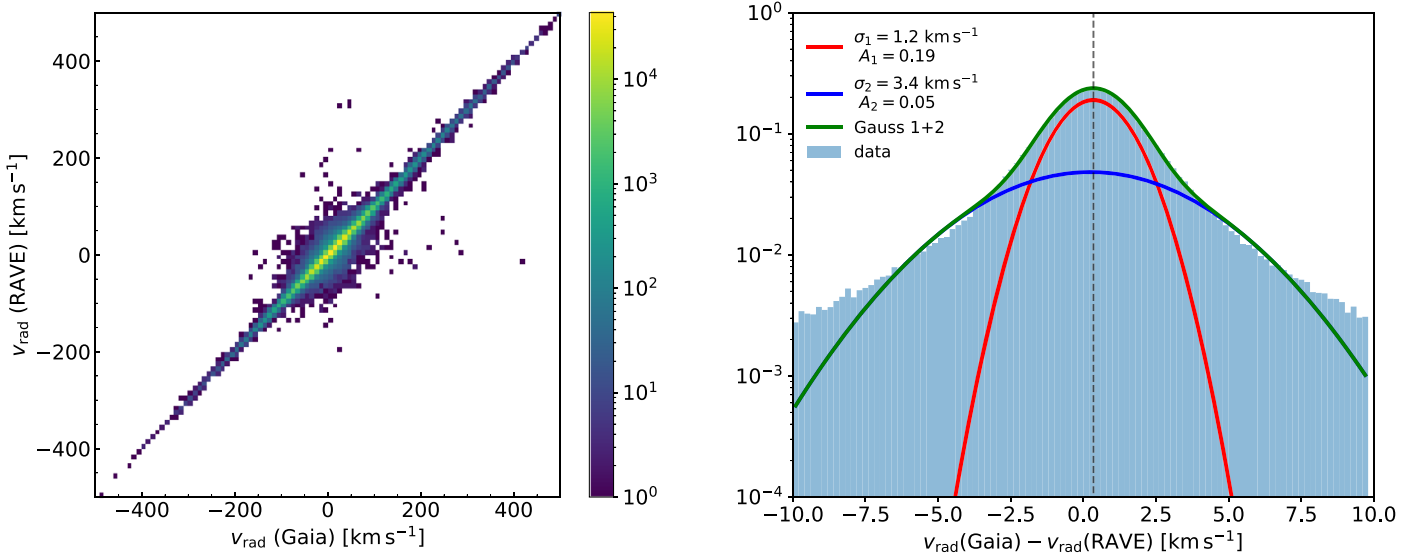


Figure 9. Left: RV derived from RAVE DR6 vs. those from Gaia DR2. Right: distribution of RV differences between Gaia DR2 and RAVE DR6. The green line compares this distribution function with a fit using two Gaussians with a standard deviation of 1.2 km s^{-1} (red) and 3.4 km s^{-1} (blue).

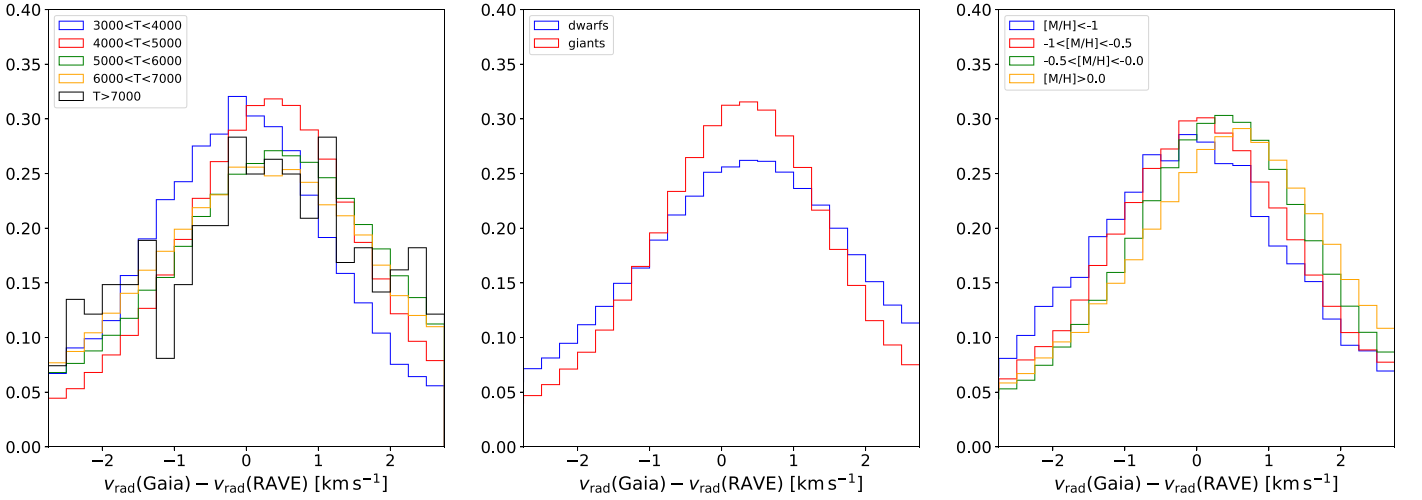


Figure 10. Radial velocity differences between RAVE DR6 and Gaia DR2 as a function of BDASP stellar parameters and MADERA $[M/H]$. Left: temperature; middle: giants ($\log g < 3.5$) vs. dwarfs ($\log g \geq 3.5$); right: metallicity.

observations of the same object (see Section 2.7). In the following analysis we calculate for each star k that has $N_{\text{repeat}}^k > 1$ observations, that fulfils the quality threshold for the RV00 sample, and that has a match in the Gaia DR2 catalog the difference between the RV determined from observation i ($1 \leq i \leq N_{\text{repeat}}^k$) and the mean \overline{RV}^k for the respective repeat sequence. This corresponds to a total of 95,068 spectra, or about 18% of the total RAVE database. We determine the uncertainty ΔRV in the RV using three methods:

1. from internal errors: ΔRV^k for star k is randomly sampled assuming a normal distribution with a width corresponding to the internal error estimate ϵ_{HRV}^k ;
2. from repeat observations: the difference ΔRV_i^k between the RV of star k determined from observation i ($1 \leq i \leq N_{\text{repeat}}^k$), RV_i^k , and the mean \overline{RV}^k for the respective repeat sequence;
3. from comparison with Gaia DR2: the difference between the RV from Gaia DR2 and that of RAVE DR6.

We then analyze the distribution function over all stars and observations and approximate it by two Gaussians using a least-squares fit analogously to Section 6.1.

The top row of Figure 11 shows the distribution function in RV for the aforementioned sample for three different methods in the left, middle, and right column, respectively. Furthermore we show the same analysis separated into giants (52,405 spectra, middle row) and dwarfs (42,663 objects, bottom row). In each panel a fit of the distribution with two Gaussians is shown.

The comparison between the repeat sequence and the internal error distributions gives very consistent results, basically resulting in very similar values for both fitting Gaussian for each of the three samples (all, giants, dwarfs).

The comparison with Gaia RVs finds identical fitting parameters as in Figure 9, indicating no systematic difference between the repeat sample studied here and the full RV00 data set. The width of the narrower Gaussians is a factor of 1.4 larger; the factor of the wider Gaussian is typically somewhat

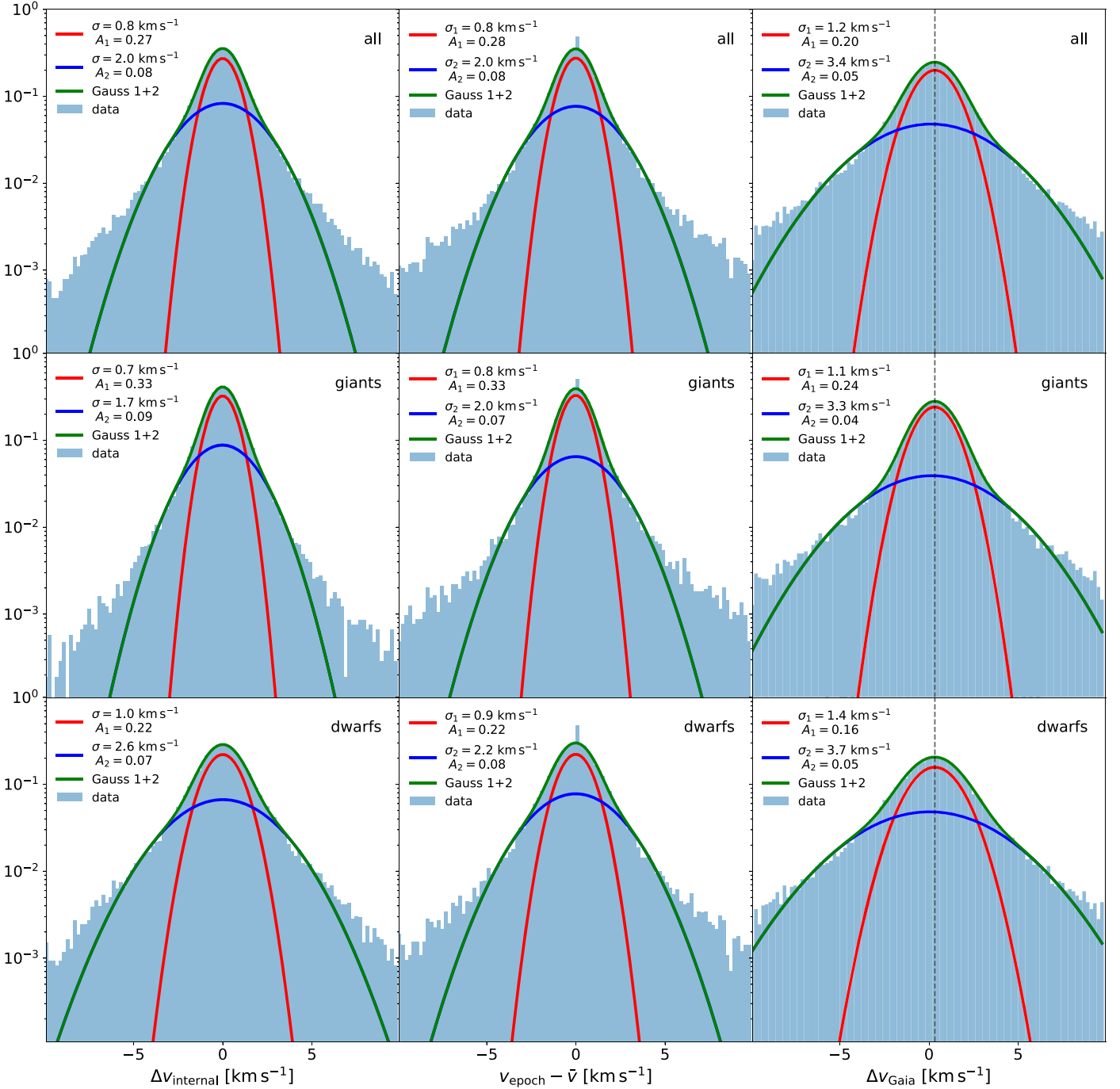


Figure 11. Difference in the RV for all stars (top row), dwarfs (medium row), and giants (bottom row) with more than one observation. The left column shows the distribution of the expected velocity difference if the RV^k for each star k is normally distributed with variance ϵ_{HRV}^k . The middle column shows the difference of the RV_i^k of star k measured at epoch i against \bar{RV}^k , the RV averaged over all epochs available for star k . The right column shows a comparison between the RV measured by Gaia and that measured by RAVE. The red and blue curves correspond to the individual Gaussians of a two-Gaussian fit to the distribution, shown in green.

higher. This behavior is in very good agreement with our expectation: for two independent observations of similar uncertainty (which is what we would expect for Gaia and RAVE considering the comparable resolution and S/N), the errors should add in quadrature, resulting in a $\sqrt{2}$ wider distribution function.³⁹

³⁹ Note that for the repeat sequence the difference at one epoch to the mean is taken rather than the difference between the velocities at two observation epochs. In the latter case we get the same $\sqrt{2}$ factor.

The fit by two Gaussians should be merely seen as a simple model to approximate a distribution function which cannot be approximated by a single normal distribution but exhibits considerable non-normal wings. The reasons for these wings are manifold and include: (i) poorer fits in general for dwarf than for giants; (ii) a systematic decrease in accuracy toward higher temperatures owing to the less prominent Ca triplet feature; (iii) objects with intrinsically variable RVs, as the observation epochs of RAVE and Gaia DR2 data are between a few days and up to 12 yr apart; (iv) varying presence of

Table 6
DR6_SPARV Catalog Description

Col	Format	Units	NULL	Label	Explanations
1	char	...	N	rave_obs_id	RAVE spectrum designation ^a
2	char	...	N	raveid	RAVE target designation ^b
3	char	...	N	objectid	object identifier used in input catalog ^c
4	float	km s ⁻¹	N	hrv_sparv	Heliocentric RV (HRV)
5	float	km s ⁻¹	N	hrv_error_sparv	HRV error
6	float	...	N	correlation_coeff_sparv	Tonry–Davis <i>R</i> correlation coefficient
7	float	...	N	correction_rv_sparv	zero-point correction of the HRV
8	float	...	N	chisq_sparv	χ^2 of the SPARV pipeline
9	float	...	N	snr_med_sparv	median S/N ^d

Notes.

^a Observation date, field name, fiber number.

^b J2000 GCS R.A. and decl.

^c Tycho-2, SSS, DENIS.

^d As derived from SPARV, see Section 3.2.

emission-line features for active stars that can vary on similar timescales; (v) objects with a large mismatch between the observed spectrum and its best synthetic counterparts. The last can be a consequence of inadequate modeling of certain types of spectra but also poor observing conditions or suboptimal instrument performance. We note that the last is more common for stars observed through fiber numbers 1–2, or 145–150, i.e., those at the extreme edges of the CCD. Consistent with the assumptions (iv) and (v) we also find the wings of the distribution function to be less pronounced and the wider Gaussian to be somewhat suppressed for subsamples limited to high S/N.

Based on this analysis we conclude that 68% of the RVs on RAVE DR6 have a velocity accuracy better than 1.4 km s⁻¹, while 95% of the objects have RVs better than 4.0 km s⁻¹.

7. The Sixth RAVE Public Data Release: Catalog Presentation I

RAVE DR6 spectra and derived quantities are made available through a database accessible via doi:[10.17876/rave/dr.6](https://doi.org/10.17876/rave/dr.6). Since key words and unquoted identifiers are case insensitive in SQL, in general lower-case identifiers are used in the database. The two main identifiers are `rave_obs_id` and `raveid`: the former, `rave_obs_id`, is the unique identifier denoting the observation of a particular spectrum—the name is a composite of the observing date, field name, and fiber number allocated to the star on that occasion.

`raveid` is the unique identifier of the target star, the name being a composite of the target’s Galactic coordinates in the J2000.0 system. Consequently, objects that have several observations have the same `raveid` for all, but differ in their `rave_obs_id`. The database contains also a considerable number of auxiliary parameters that can be employed to further scrutinize the specifics of the reductions using the various pipelines. These variables are described on the aforementioned website. Furthermore, ample information regarding cross-identification with other catalogs is given.

For convenience we also provide a set of FITS, CSV, and HDF files of the overall RAVE catalog, featuring key variables sufficient for the majority of applications of the RAVE survey. These data are organized in 16 files according to the pipeline employed; the content for six of these files is briefly described in the following paragraphs and associated tables; for the remaining 10 we refer to

paper DR6-2. We avoid duplication of variable entries in the different files, with the exception of `rave_obs_id`, which can be used to link the contents of the various catalogs.

7.1. The RAVE DR6 Catalog of Spectra

RAVE spectra and error spectra are available via the database on the RAVE webpage⁴⁰ (DR6_Spectra, doi:[10.17876/rave/dr.6/019](https://doi.org/10.17876/rave/dr.6/019)). Spectra are made available in FITS files with a name based on their `rave_obs_id` containing (i) the actual wavelength-calibrated and flux-normalized spectrum and (ii) the associated error spectrum (for example, see Figure 6).

Only spectra that successfully passed the SPARV pipeline (i.e., where an RV can be derived) are added to the database.

7.2. The RAVE DR6 Catalog of Radial Velocities

The DR6_SPARV table (doi:[10.17876/rave/dr.6/001](https://doi.org/10.17876/rave/dr.6/001), Table 6) should be seen as the master file of the RAVE DR6 data release. It contains all observations and objects for which a spectrum can be found in the spectral database, contains all observations for which the pipeline converged to provide an RV, and is the sample of spectra that served as input for further analysis pipelines, e.g., those to derive stellar atmospheric parameters or abundances.

DR6_SPARV contains the heliocentric RV, information on the zero-point calibration using sky lines (see Section 5) and convergence information of the pipeline (Table 6). In the RAVE database, additional information such as stellar parameters from matching templates is provided (DR6_SPARV_aux, doi:[10.17876/rave/dr.6/002](https://doi.org/10.17876/rave/dr.6/002)). These data should, if at all, be used with care for further astrophysical applications, as they are subject to complicated biases (see DR4 Section 4.4).

7.3. The RAVE DR6 Catalog of Diagnostic Data

DR6_ObsData (doi:[10.17876/rave/dr.6/003](https://doi.org/10.17876/rave/dr.6/003)) contains helpful diagnostic information regarding the RAVE data and the derived data products (Table 7). This includes, e.g., the observing date, exposure time, fiber number, field plate used, number of arc lines used for the wavelength calibration, the coordinates of the field plate center, phase of Moon, and healpix coordinates.

⁴⁰ <http://www.rave-survey.org>

Table 7
DR6_ObsData Catalog Description

Col	Format	Units	NULL	Label	Explanations
1	char	...	N	rave_obs_id	RAVE spectrum designation
2	char	deg	N	ra_input	R.A. in input catalog
3	char	deg	N	dec_input	decl. in input catalog
4	char	...	N	field	field denotator, composite of obsdate and fieldname
5	int	...	N	obsdate	Observation date yyyyymmdd
6	char	...	N	fieldname	name of the field: R.A. and decl. of field center
7	char	...	N	fibernumber	Number of optical fiber [1,150]
8	char	...	N	ut_start	exposure start in Coordinated Universal Time
9	char	...	N	ut_end	exposure end in Coordinated Universal Time
10	char	...	N	lst_start	exposure start in Local Sidereal Time
11	char	...	N	lst_end	exposure end in Local Sidereal Time
12	int	s	N	exposure_time	total exposure time
13	char	deg	N	ra_field	R.A. field center
14	char	deg	N	dec_field	decl. field center
15	int	...	N	platenumber	Number of field plate [1..3]
16	float	...	N	airmass	Airmass
17	float	...	Y	lunar_phase	Lunar phase
18	char	...	N	healpix4096	HEALPix value ^a
19	int	...	Y	cluster_flag	1: targeted observation, NULL: otherwise
21	int	...	Y	footprint_flag	1: star in the RAVE footprint, NULL: otherwise

Note.

^a Hierarchical Equal-Area isoLatitude Pixelisation (HEALPix) values were computed using the resolution parameter $N_{\text{side}} = 4096$ (resolution index of 12) and the NESTED numbering scheme. Any lower-resolution index HEALPix value can be computed from the given one by dividing it by $4^{(12-n)}$, where $n < 12$ is the desired resolution index.

Table 8
DR6_Class Catalog Description

Col	Format	Units	NULL	Label	Explanations
1	char	...	N	rave_obs_id	RAVE spectrum designation
2	char	...	N	flag1_class	Primary flag
3	char	...	Y	flag2_class	Secondary flag
4	char	...	Y	flag3_class	Tertiary flag
5	float	...	N	w1_class	Weight associated with primary flag
6	float	...	Y	w2_class	Weight associated with secondary flag
7	float	...	Y	w3_class	Weight associated with tertiary flag

7.4. The RAVE DR6 Catalog of Classification

Results of the automated classification (Section 4) are assembled in the DR6_Class file (doi:10.17876/rave/dr.6/004, Table 8), giving up to three classification flags and their relative weights.

7.5. The RAVE DR6 Catalog of Repeat Observations

To enable an easy analysis of stars with more than one observation date, the DR6_Repeats file (doi:10.17876/rave/dr.6/005, Table 9) features the raveid to identify the target uniquely, the number of revisits n_Repeats, and the respective rave_obs_ids of all observations of that particular target (for a detailed analysis, see Section 2.7).

7.6. Cross-match of RAVE DR6 with Gaia DR2 and Other Catalogs

The RAVE DR6 data release is complemented by two files cross-matching RAVE DR6 with Gaia DR2 (DR6_GaiaDR2, doi:10.17876/rave/dr.6/015) and with a suite of other catalogs

Table 9
DR6_Repeats Catalog Description

Col	Format	NULL	Label	Explanations
1	char	N	raveid	Unique object identifier
2	int	N	n_repeats	number of repeat observations (between 1 and 13)
3-15	char	Y	rave_obs_id1 - rave_obs_id13	unique spectrum identifiers for all repeat observations

including Tycho-2, 2MASS, WISE, APASS9, and SKY-MAPPER (DR6_XMatch, doi:10.17876/rave/dr.6/016).

8. Summary and Conclusions

The RAVE final data release concludes a more than 15 year effort to provide a homogeneous data set for Galactic archeology studies. RAVE DR6 presents spectra and RVs for individual stars in the magnitude range $9 < I < 12$ mag. The spectra cover a wavelength range of 8410–8795 Å at an average resolution of $R \sim 7500$. The RAVE catalog can be

accessed via doi:[10.17876/rave/dr.6/001](https://doi.org/10.17876/rave/dr.6/001). The typical S/N of a RAVE star is 40, and the typical uncertainty in RV is $<2 \text{ km s}^{-1}$. Catalogs containing observing statistics, repeat observations, an automated classification scheme, and cross-matches with the Gaia DR2 and other catalogs such as 2MASS, DENIS, HIPPARCOS, TYCHO2, WISE, SKYMAPPER, and APASS9 complement the RAVE final data release. Accompanying derived data products such as stellar parameters, chemical abundances, and distances as well as some science applications are presented in Paper DR6-2.

Major scientific projects like the RAVE survey are made possible by the contributions of many, in particular those of graduate students and postdocs. This final data release is published in memory of one of the first and most active student participants in RAVE, Gregory R. Ruchti (1980–2019), whose life was taken far too early. His enthusiasm and dedication were key elements of the success of the RAVE collaboration and his contributions live on in the discoveries that are enabled by the RAVE data.

Funding for RAVE has been provided by: the Leibniz-Institut für Astrophysik Potsdam (AIP); the Australian Astronomical Observatory; the Australian National University; the Australian Research Council; the French National Research Agency (Programme National Cosmology et Galaxies (PNCG) of CNRS/INSU with INP and IN2P3, co-funded by CEA and CNES); the German Research Foundation (SPP 1177 and SFB 881: Project-ID 138713538); the European Research Council (ERC-StG 240271 Galactica); the Istituto Nazionale di Astrofisica at Padova; The Johns Hopkins University; the National Science Foundation of the USA (AST-0908326); the W. M. Keck foundation; the Macquarie University; the Netherlands Research School for Astronomy; the Natural Sciences and Engineering Research Council of Canada; the Slovenian Research Agency (research core funding no. P1-0188); the Swiss National Science Foundation; the Science & Technology Facilities Council of the UK; Opticon; Strasbourg Observatory; and the Universities of Basel, Groningen, Heidelberg and Sydney. P.J.M. is supported by grant 2017-03721 from the Swedish Research Council. L.C. is the recipient of the ARC Future Fellowship FT160100402. R.A.G. acknowledges the support from the PLATO CNES grant. S.M. would like to acknowledge support from the Spanish Ministry with the Ramon y Cajal fellowship number RYC-2015-17697. M.V. acknowledges support of the Deutsche Forschungsgemeinschaft (DFG, project number: 428473034). M.S. thanks Research School of Astronomy & Astrophysics in Canberra for support through a Distinguished Visitor Fellowship. R.F.G.W. thanks the Kavli Institute for Theoretical Physics and the Simons Foundation for support as a Simons Distinguished Visiting Scholar. This research was supported in part by the National Science Foundation under grant No. NSF PHY-1748958 to KITP.

This work has made use of data from the European Space Agency (ESA) mission Gaia (<https://www.cosmos.esa.int/gaia>), processed by the Gaia Data Processing and Analysis Consortium (DPAC, <https://www.cosmos.esa.int/web/gaia/dpac/consortium>). Funding for the DPAC has been provided by national institutions, in particular the institutions participating in the Gaia Multilateral Agreement.

Software: HEALPix (Górski et al. 2005), IRAF (Tody 1993), Matplotlib (Hunter 2007), numpy (Oliphant 2006), pandas (McKinney 2010), RVSAO (Mink & Kurtz 1998).

Appendix Bookkeeping of RAVE Observations

In total there are 7041 RAVE DR5 spectra that are not in this final data release. These fall into the following two categories.

1. Fewer than four arc lines were available for wavelength calibrations. This condition mainly occurs near the edges of the field plate owing to the fast focal ratio of the spectrograph camera when many fibers have been broken (Steinmetz et al. 2018) (687 spectra).
2. Cases where the processing failed or the corresponding error spectrum could not be computed (6434 spectra).

Furthermore, 4727 spectra were added that are not in RAVE DR5, mainly corresponding to targeted observations in the context of the Aquarius substructure (Williams et al. 2011).

ORCID iDs

Matthias Steinmetz  <https://orcid.org/0000-0001-6516-7459>
Gal Matijević  <https://orcid.org/0000-0002-6070-2288>
Harry Enke  <https://orcid.org/0000-0002-2366-8316>
Tomaž Zwitter  <https://orcid.org/0000-0002-2325-8763>
Guillaume Guiglion  <https://orcid.org/0000-0002-1317-2798>
Paul J. McMillan  <https://orcid.org/0000-0002-8861-2620>
Georges Kordopatis  <https://orcid.org/0000-0002-9035-3920>
Marica Valentini  <https://orcid.org/0000-0003-0974-4148>
Cristina Chiappini  <https://orcid.org/0000-0003-1269-7282>
Luca Casagrande  <https://orcid.org/0000-0003-2688-7511>
Jennifer Wojno  <https://orcid.org/0000-0002-3233-3032>
Borja Anguiano  <https://orcid.org/0000-0001-5261-4336>
Olivier Bienaymé  <https://orcid.org/0000-0002-4605-865X>
James Binney  <https://orcid.org/0000-0002-1926-2436>
Donna Burton  <https://orcid.org/0000-0002-3939-8808>
Patrick de Laverny  <https://orcid.org/0000-0002-2817-4104>
Kenneth Freeman  <https://orcid.org/0000-0001-6280-1207>
Brad K. Gibson  <https://orcid.org/0000-0003-4446-3130>
Gerard Gilmore  <https://orcid.org/0000-0003-4632-0213>
Eva K. Grebel  <https://orcid.org/0000-0002-1891-3794>
Amina Helmi  <https://orcid.org/0000-0003-3937-7641>
Andrea Kunder  <https://orcid.org/0000-0002-2808-1370>
Ulisse Munari  <https://orcid.org/0000-0001-6805-9664>
Quentin Parker  <https://orcid.org/0000-0002-2062-0173>
Gregory R. Ruchti  <https://orcid.org/0000-0003-0631-912X>
George M. Seabroke  <https://orcid.org/0000-0003-4072-9536>
Milorad Stupar  <https://orcid.org/0000-0002-0338-9539>
Fred Watson  <https://orcid.org/0000-0002-3590-3547>
Rosemary F. G. Wyse  <https://orcid.org/0000-0002-4013-1799>
Friedrich Anders  <https://orcid.org/0000-0003-4524-9363>
Teresa Antoja  <https://orcid.org/0000-0003-2595-5148>
Danijela Birko  <https://orcid.org/0000-0002-5571-5981>
Joss Bland-Hawthorn  <https://orcid.org/0000-0001-7516-4016>
Diego Bossini  <https://orcid.org/0000-0002-9480-8400>
Rafael A. García  <https://orcid.org/0000-0002-8854-3776>
Ismael Carrillo  <https://orcid.org/0000-0002-0759-0766>
William J. Chaplin  <https://orcid.org/0000-0002-5714-8618>
Benoit Famaey  <https://orcid.org/0000-0003-3180-9825>
Ortwin Gerhard  <https://orcid.org/0000-0003-3333-0033>
Paula Jofre  <https://orcid.org/0000-0002-0722-7406>

Andreas Just <https://orcid.org/0000-0002-5144-9233>
 Savita Mathur <https://orcid.org/0000-0002-0129-0316>
 Andrea Miglio <https://orcid.org/0000-0001-5998-8533>
 Ivan Minchev <https://orcid.org/0000-0002-5627-0355>
 Benoit Mosser <https://orcid.org/0000-0002-7547-1208>
 Thaise S. Rodrigues <https://orcid.org/0000-0002-9414-339X>
 Ralf-Dieter Scholz <https://orcid.org/0000-0002-0894-9187>
 Sanjib Sharma <https://orcid.org/0000-0002-0920-809X>

References

- Bastian, U., Röser, S., & Scholz, R. D. 2001, in ASP Conf. Ser. 228, Dynamics of Star Clusters and the Milky Way, ed. S. Deiters et al. (San Francisco, CA: ASP), 321
- Bessell, M. S. 1979, *PASP*, 91, 589
- Binney, J., Burnett, B., Kordopatis, G., et al. 2014, *MNRAS*, 437, 351
- Blair, M., & Gilmore, G. 1982, *PASP*, 94, 742
- Bland-Hawthorn, J., & Gerhard, O. 2016, *ARA&A*, 54, 529
- Boeche, C., Siebert, A., Williams, M., et al. 2011, *AJ*, 142, 193
- Breddels, M. A., Smith, M. C., Helmi, A., et al. 2010, *A&A*, 511, A90
- Burnett, B., Binney, J., Sharma, S., et al. 2011, *A&A*, 532, A113
- Casey, A. R., Hawkins, K., Hogg, D. W., et al. 2017, *ApJ*, 840, 59
- Cropper, M., Katz, D., Sartoretti, P., et al. 2018, *A&A*, 616, A5
- DENIS Consortium 2005, *yCat*, 2236, 0
- De Silva, G. M., Freeman, K. C., Bland-Hawthorn, J., et al. 2015, *MNRAS*, 449, 2604
- Epchtein, N., de Batz, B., Capoani, L., et al. 1997, *Msngr*, 87, 27
- ESA 1997, The Hipparcos and Tycho Catalogues (Noordwijk: ESA)
- Freeman, K., & Bland-Hawthorn, J. 2002, *ARA&A*, 40, 487
- Gaia Collaboration, Brown, A. G. A., Vallenari, A., et al. 2018, *A&A*, 616, A1
- Gilmore, G., Randich, S., Asplund, M., et al. 2012, *Msngr*, 147, 25
- Górski, K. M., Hivon, E., Banday, A. J., et al. 2005, *ApJ*, 622, 759
- Hambly, N. C., MacGillivray, H. T., Read, M. A., et al. 2001, *MNRAS*, 326, 1279
- Høg, E., Fabricius, C., Makarov, V. V., et al. 2000, *A&A*, 355, L27
- Hunter, J. D. 2007, *CSE*, 9, 90
- Jofré, P., Heiter, U., & Soubiran, C. 2019, *ARA&A*, 57, 571
- Johnston, K. J. 2003, *Proc. SPIE*, 4854, 303
- Jones, D. H., Read, M. A., Saunders, W., et al. 2009, *MNRAS*, 399, 683
- Kordopatis, G., Gilmore, G., Steinmetz, M., et al. 2013, *AJ*, 146, 134
- Kos, J., Bland-Hawthorn, J., Betters, C. H., et al. 2018, *MNRAS*, 480, 5475
- Kos, J., Lin, J., Zwitter, T., et al. 2017, *MNRAS*, 464, 1259
- Kunder, A., Kordopatis, G., Steinmetz, M., et al. 2017, *AJ*, 153, 75
- Lewis, I. J., Cannon, R. D., Taylor, K., et al. 2002, *MNRAS*, 333, 279
- Lindgren, L., Lammers, U., Bastian, U., et al. 2016, *A&A*, 595, A4
- Majewski, S. R., Schiavon, R. P., Frinchaboy, P. M., et al. 2017, *AJ*, 154, 94
- Matijević, G., Chiappini, C., Grebel, E. K., et al. 2017, *A&A*, 603, A19
- Matijević, G., Zwitter, T., Bienaymé, O., et al. 2012, *ApJS*, 200, 14
- McKinney, W. 2010, in Proc. 9th Python in Science Conf., ed. S. van der Walt & J. Millman (Austin, TX: SciPy), 56
- McMillan, P. J., Kordopatis, G., Kunder, A., et al. 2018, *MNRAS*, 477, 5279
- Mink, D. J., & Kurtz, M. J. 1998, in ASP Conf. Ser. 145, Astronomical Data Analysis Software and Systems VII, ed. R. Albrecht, R. N. Hook, & H. A. Bushouse (San Francisco, CA: ASP), 93
- Miszalski, B., Shortridge, K., Saunders, W., Parker, Q. A., & Croom, S. M. 2006, *MNRAS*, 371, 1537
- Munari, U., Henden, A., Frigo, A., et al. 2014, *AJ*, 148, 81
- Munari, U., Sordo, R., Castelli, F., & Zwitter, T. 2005, *A&A*, 442, 1127
- Nordström, B., Mayor, M., Andersen, J., et al. 2004, *A&A*, 418, 989
- Oliphant, T. E. 2006, A Guide to NumPy, Vol. 1 (Spanish Fork, UT: Trelgol Publishing)
- Recio-Blanco, A., de Laverny, P., Allende Prieto, C., et al. 2016, *A&A*, 585, A93
- Rickman, H. 2001, in Proc. 24th General Assembly, Trans. of the IAU, ed. H. Rickman (San Francisco, CA: ASP), 91
- Sartoretti, P., Katz, D., Cropper, M., et al. 2018, *A&A*, 616, A6
- Siebert, A., Williams, M. E. K., Siviero, A., et al. 2011, *AJ*, 141, 187
- Skrutskie, M. F., Cutri, R. M., Stiening, R., et al. 2006, *AJ*, 131, 1163
- Steinmetz, M. 2003, in ASP Conf. Ser. 298, GAIA Spectroscopy: Science and Technology, ed. U. Munari (San Francisco, CA: ASP), 381
- Steinmetz, M., Guiglion, G., McMillan, P. J., et al. 2020, *AJ*, 160, 83
- Steinmetz, M., Zwitter, T., Matijević, G., Siviero, A., & Munari, U. 2018, *RNAAS*, 2, 194
- Steinmetz, M., Zwitter, T., Siebert, A., et al. 2006, *AJ*, 132, 1645
- Tody, D. 1993, in ASP Conf. Ser. 52, Astronomical Data Analysis Software and Systems II, ed. R. J. Hanisch, R. J. V. Brissenden, & J. Barnes (San Francisco, CA: ASP), 173
- Valentini, M., Chiappini, C., Davies, G. R., et al. 2017, *A&A*, 600, A66
- Watson, F. G., Parker, Q. A., Bogatu, G., et al. 2000, *Proc. SPIE*, 4008, 123
- Williams, M. E. K., Steinmetz, M., Sharma, S., et al. 2011, *ApJ*, 728, 102
- Wojno, J., Kordopatis, G., Piffl, T., et al. 2017, *MNRAS*, 468, 3368
- Yanny, B., Rockosi, C., Newberg, H. J., et al. 2009, *AJ*, 137, 4377
- Žerjal, M., Zwitter, T., Matijević, G., et al. 2013, *ApJ*, 776, 127
- Žerjal, M., Zwitter, T., Matijević, G., et al. 2017, *ApJ*, 835, 61
- Zhao, G., Zhao, Y.-H., Chu, Y.-Q., Jing, Y.-P., & Deng, L.-C. 2012, *RAA*, 12, 723
- Zwitter, T., Kos, J., Chiavassa, A., et al. 2018, *MNRAS*, 481, 645
- Zwitter, T., Matijević, G., Breddels, M. A., et al. 2010, *A&A*, 522, A54
- Zwitter, T., Siebert, A., Munari, U., et al. 2008, *AJ*, 136, 421